Research Performance Progress Report (RPPR) for DOE/EERE

Project Title:	Second Generation Novel High Temperature Commercial Receiver & Low Cost High Performance Mirror Collector for Parabolic Solar Trough
Covering Period:	October 1, 2014 to November 30, 2015
Approved Project Period:	October 1, 2014 to November 30, 2015
Submission Date:	February 29, 2016
Recipient:	Garrett Nilsen SunShot Initiative Office 950 L'Enfant Plaza Washington, DC
Website (if available)	www.norwichtech.com
Award Number:	**DE-EE0006687**
Working Partners:	**Creare, Inc.; UCSD; Gossamer**
Cost-Sharing Partners:	
PI:	Name: Joel Stettenheim Position title: President Phone: 802-384-1333 Email: Stettenheim@norwitech.com
Submitted by:	Name (if other than PI) Position title Phone: Email:

DOE Project Team:	Contract Specialist	-	Jeremy Mikrut
	Program Manager	-	Victor Kane
	Technical Manager	-	Garrett Nilsen

February 29, 2016

Signature Date

Executive Summary:

Norwich Technologies (NT) is developing a disruptively superior solar field for trough concentrating solar power (CSP). Troughs are the leading CSP technology (85% of installed capacity), being highly deployable and similar to photovoltaic (PV) systems for siting. NT has developed the SunTrap receiver, a disruptive alternative to vacuum-tube concentrating solar power (CSP) receivers, a market currently dominated by the Schott PTR-70. The SunTrap receiver will (1) operate at higher temperature (*T*) by using an insulated, recessed radiation-collection system to overcome the energy losses that plague vacuum-tube receivers at high *T*, (2) decrease acquisition costs via simpler structure, and (3) dramatically increase reliability by eliminating vacuum. It offers comparable optical efficiency with thermal loss reduction from ≥ 26% (at presently standard *T*) to ≥ 55% (at high *T*), lower acquisition costs, and near-zero O&M costs.

In conjunction with advancing its SunTrap receiver technology, NT is developing a low-cost, high-performance parabolic trough mirror collector using a suspension structure. The strong performance of the SunTrap receiver and suspension mirror collector has been successfully demonstrated under the current award. As discussed herein, the receiver has achieved aggressive thermal loss targets of less than 440 W/m at 550 °C absorber temperature and the suspension mirror has achieved optical errors of less than 5 mrad and optical efficiencies of > 75%. This demonstrated performance well positions the SunTrap receiver and suspension mirror for strong commercial growth.

NT's disruptive technology marshals diverse advances in design, materials and coatings to revolutionize aspects of the CSP trough solar field. By enabling significant operational and cost advances in the most trusted and broadly implemented form of CSP, solar trough, this technology has the prospect for rapid, widespread adoption. By improving performance while reducing acquisition and O&M costs, NT's proposed parabolic-trough receiver-mirror pair contributes importantly to reaching the SunShot goal of 6 ¢/kWh LCOE for CSP. The significantly more efficient, higher-*T* operation and reduced complexity of NT's SunTrap system are improvements additional to those identified for parabolic receivers by the SunShot Vision Study and the DOE's Line-Focus Solar Power Plant Cost Reduction Plan.

Project Overview:

Our SunShot Incubator project builds directly on the expertise and resources from previous work in which we (1) developed and validated optical and thermal models and completed rigorous optimization analyses to identify key performance characteristics as part of developing first-generation laboratory prototype designs, (2) built optical and thermal laboratory prototypes and test systems with associated innovative testing protocols, and (3) performed extensive testing of our prototypes. For the present project**,** we are (1) fully optimizing, designing, building, and testing our second-generation prototype receiver based on results from our first-generation prototype, showing additional performance improvements, and (2) developing a low-cost, high-performance parabolic suspension trough mirror collector that leverages the unique structural opportunities enabled by our SunTrap receiver (see Figure 1). In addition, we are continuing our business development and marketing work to bring to market our unique solution to low-cost CSP.

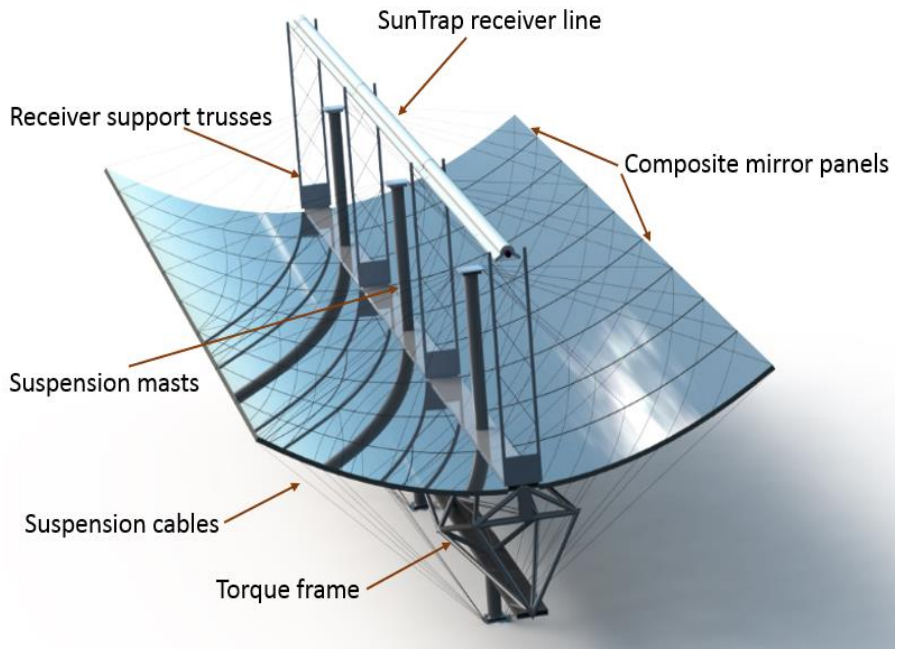

Fig. 1. Rendering of a Suntrap receiver line installed on a suspension mirror structure. The receiver consists of a central absorber tube with air-stable solar selective coating, high temperature insulation, shell, and glass window. The collector is built of highly stiff composite-backed mirror panels anchored to a torque frame at their inner edges and supported by suspension cables at corners and midpoints. Accurate optical shape is maintained by tensioned cables on front and back of mirror. Masts provide anchor points for cables and are stiff in bending to preserve accuracy. The torque frame acts as a structural backbone for the collector, resisting twist and bending in the structure to maintain alignment of receiver and mirror. Lightweight plane trusses support the receiver line.

We have successfully performed testing of the suspension collector optical accuracy and SunTrap receiver optical and thermal performance. In Q1, we developed modeling capabilities and in-depth design knowledge for the suspension trough collector, and developed a draft design that meets performance targets. On the receiver side, we performed further geometric optimizations for high-temperature performance. In Q2, we defined the prototype designs for the suspension collector and optical and thermal test receivers, as well as planned test protocols for mirror characterization and optical/thermal efficiency. In Q3, we moved prototype designs into manufacturing and refined test procedures. In Q4, we finalized prototype assembly and performed the optical and thermal testing, demonstrating receiver and collector system performance at prototype scale.

Statement of Project Objectives (SOPO) Task Summary:

Task 1 – **High Temperature Receiver Design**

NT modeled new geometric configurations of the SunTrap receiver in order to establish co-optimized optical and thermal performance. Studies included both pure performance optimization and improvement of material use, especially with regard to efficient distribution of insulation around the receiver tube and air cavity. The resulting design is optimized for field service at a peak temperature of 550 °C. The initial prototype receiver geometry is based on a 3.5 in (88.9 mm) O.D. stainless steel 316L absorber tube. The absorber tube is partially covered by microporous insulation that is wrapped in stainless steel foil, with the remaining (exposed) tube surface coated with an air-stable solar selective coating. A protective shell of 304 stainless steel houses the insulation and provides attachment to the glass window by means of stainless steel

clips and ceramic-fiber sealing strips. The profile of the shell, composed of two congruent halves, is governed by the optimized thickness of insulation surrounding the absorber tube and by the geometry of the cavity. The depth of the cavity is optimized for thermal performance and the angle between the bounding planar surfaces of insulation is controlled by the rim angle of the mirror collector.

Subtask 1.1 - Thermal Analysis of High Temperature Receiver

The thermal performance was modeled using ANSYS FLUENT. The aim of this analysis was to calculate heat loss for various receiver diameters using the design principles that were discovered from the first-gen prototype and deliverables D0. In this analysis it was assumed that for each receiver geometry microporous insulation of thickness t_i covered fraction $s_i/\pi d$ of the surface of an absorber tube having diameter d, the remainder of the absorbing surface being coated with a solar-selective coating that has an emissivity comparable to that used on the Schott PTR-70. NT has developed a receiver cost-performance model to guide material choices and refine design; for operation in the 550-650 °C peak temperature range, thickness t_i^* of microporous insulation around the absorber is optimal. The depth h_c of the air cavity was constant. The heat loss for varying temperatures and absorber opening widths is shown in Figure 2. To satisfy heat loss deliverables, the absorber opening width must be less than 6.3 cm (assuming a 5 m collector aperture).

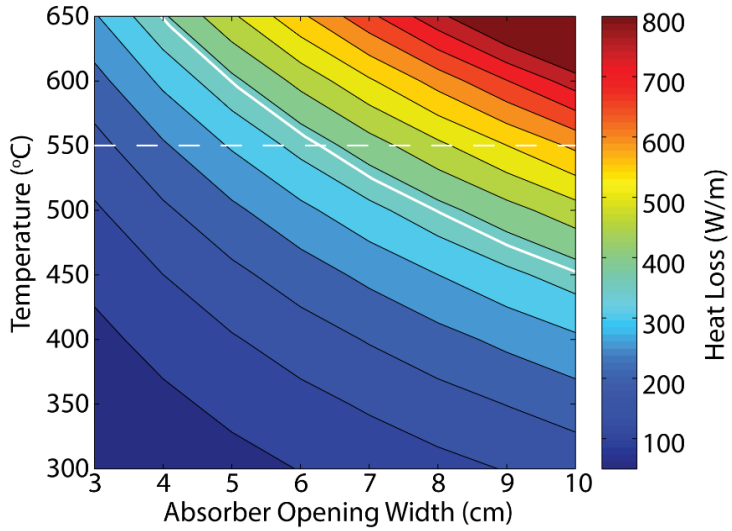

Figure 2- SunTrap heat loss for variations in absorber opening width and temperature. The solid white contour line is a constant heat loss of 380 W/m, and the dotted white line is a constant temperature of 550 °C. To satisfy the heat loss target, the heat loss must be less than 380 W/m (solid white contour line) at 550 °C (white dotted line) on a 5m aperture trough. The absorber opening width must be smaller than the absorber width at the intersection of these 2 lines (~6.3 cm).

Subtask 1.2 - Optical Analysis of High Temperature Receiver

The optical performance of the receiver is analyzed using a proprietary ray tracing program that has been validated against the model developed by *Cheng et al.*, [2014] (*Comparative and sensitive analysis for parabolic trough solar collectors with a detailed Monte Carlo ray-tracing optical model, Applied Energy, 115 (2014) 559-572*). The model used for this analysis includes a sunshape model developed by *Buie et al*, [2003] (*Sunshape distributions for terrestrial solar simulations, Solar Energy, 74 (2) 113-122(10)),* two million traced rays, a 4.5 mrad optical error budget applied as a Gaussian scatter of the reflected ray at the mirror surface, refractions due to the glass receiver envelope and losses due to imperfect reflectivity, transmittance, and absorptivity. For the initial design study a 5 m mirror aperture was assumed. Since performance is consistent for the same concentration ratio, the receiver geometry can be easily scaled to any mirror aperture. The radiation captured by the heat transfer fluid is calculated accounting for geometric losses from the ray tracing process, dirt on mirror (0.95), mirror

reflectance (0.94), glass transmittance (0.96), receiver absorptivity (0.96), dirt on receiver cover (0.98), and active area losses (0.992). It is assumed that there are no cosine losses or other incident angle modifiers.

Figure 3 demonstrates the optical efficiency for variations in rim angle and absorber opening width for the SunTrap receiver. The required 75% optical performance is represented by the bold contour line. All receiver geometries that satisfy this deliverable are located to the right of this contour. In this analysis it is assumed that the insulation covers a fraction $s_i/\pi d$ of the absorber tube. This relationship was found to produce a good co-optimization between optical and thermal performance and receiver geometry. In this system, the focal point of the mirror and the center of the absorber tube do not align. For example, through the use of ray tracing simulations, it was found that for the SunTrap receiver shown in Figure 1, the center of the absorber tube should be located off the focal point of the trough.

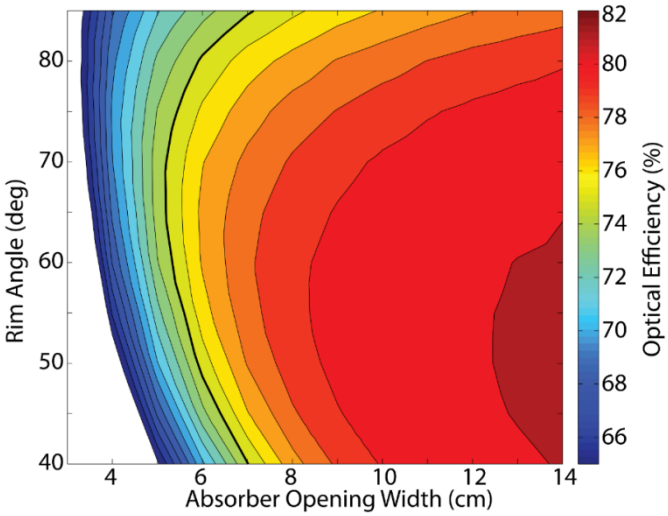

Figure 3 - Optical Performance of the SunTrap receiver for variations in rim angle and the absorber opening width. All receiver geometries that satisfy the 75% optical performance deliverable are to the right of the bold contour line.

The selected receiver geometry is a co-optimization of the optical and thermal performance to produce the maximum thermal energy output.

The overall efficiency of the SunTrap receiver was calculated as

$$\eta_{total} = (\eta_{opt} \times BNR \times W - HL)/(BNR \times W)\,,$$

where η_{total} is the overall efficiency, η_{opt} is the optical efficiency, BNR is the beam normal radiation (W/m^2), $W$is the aperture width (m), and HL is the receiver heat loss (W/m). The overall efficiency was calculated over a range of rim angles and absorber opening widths at temperatures of 400 °C, 550 °C and 650 °C (Figure 4) on a 5m mirror aperture. The BNR used was 700 W/m^2. This value represents smaller than typical design values (~900 W/m^2) but is more representative of the average annual operational conditions. Figure 4 shows that as the temperature (and heat loss) increases the optimum absorber opening width decreases. It can be noted that at higher temperatures the optimum receiver geometry uses a mirror with a larger rim angle than chosen for this design. However, at larger rim angles the receiver becomes unreasonably wide in order to maintain a constant cavity depth of h_c.

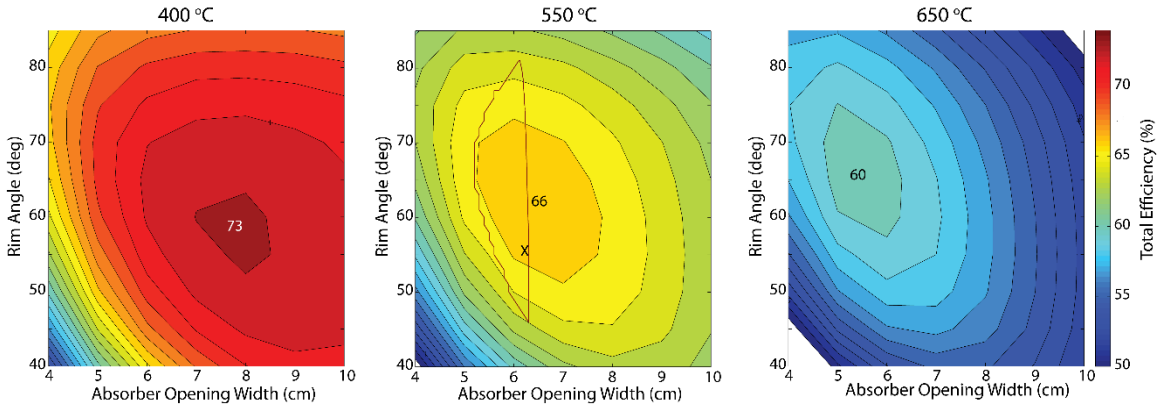

Figure 4- Total efficiency of the SunTrap receiver for variations in rim angle and absorber opening width for temperatures of 400 °C (left), 550 °C (middle) and 650 °C (right). Red contour line on 550 °C plot shows area in which both optical and heat loss deliverables are met.

Subtask 1.3 - Structural Design of High Temperature Receiver & Prototype

Receiver structural design tasks included coupling of support trusses to the receiver, allowing for thermal expansion of the absorber relative to the receiver body, and coupling of receiver support trusses to the collector. Structural analysis of the suspension collector demonstrated that separating the receiver supports from the suspension mast components reduces deflections of the assembly, and so receiver supports for this round of prototyping became simple 2D trusses attached to the collector torque tube.

Figure 5– Absorber tube support bracket assembly for thermal test prototype. Collar is cut from tubing stock, while arms are bent sheet metal. Four spacers (ceramic in heat loss prototype, PTFE in optical prototype) on screws such that tube is supported but can slide axially during heating and cooling cycles. Brackets act to stiffen shell, which in turn supports absorber tube. With a bracket every ~2 m, absorber tube deflections are reduced.

Several strategies exist for coupling the receiver body to the collector supports and handling thermal expansion of the receiver line; NT is addressing these options in full detail in concurrent work on the SolarMAT2 project (DE-EE0006813). For the purposes of performance demonstration under this award, NT chose a simple option of attaching supports rigidly to the receiver shell, then supporting the absorber tube with internal brackets that allow the absorber to slide during thermal expansion cycles; a bracket assembly for the thermal test prototype is shown in Figure 5. The absorber tube support brackets for the optical-efficiency and heat-loss test prototypes are similar, though adapted for different tube sizes. The support brackets were designed to occupy minimal space and to fit inside the shell but outside the cavity zone away from incoming radiation.

For the optical efficiency test, the test receiver was scaled down to fit the 4.65 m prototype collector aperture (chosen to use existing parabolic forms at Gossamer Space Frames facility) so as to preserve geometric optical efficiency. The absorber tube in this configuration is a 2 in Sch80 pipe (Sch80 was selected to

provide similar bending stiffness to the full-scale, thinner-wall absorber tube). The construction is otherwise similar to the thermal test prototype receiver, except the insulation is calcium silicate rather than high-performance microporous insulation. The optical efficiency test receiver length was originally designed for a ~4 m length, but further optical analysis showed a ~4.5 m overall length to be more suitable for extending the test window over a greater range of cosine angles. Extending the receiver by ~0.5 m resulted in an overall lengthening of the collector assembly to ~4.5 m, ~3.7 m of which is fitted with reflectors.

The span of the optical test receiver warranted a careful consideration of deflection and resulting optical misalignment. An error budget of ~10 mm in absorber position due to deflections was calculated from ray tracing results. This error budget includes both the deflections of the receiver support trusses connecting to the collector and of the absorber tube itself. The receiver supports were lightweight 2D trusses, which limited deflections at the receiver ends to ~3 mm. Deflection of the 2 inch Sch80 steel absorber tube was considered for two restraint cases: pinned and fixed, which were the bounding cases for the real mounting hardware. In the case of pinned restraints, the absorber tube, when filled with water, would deflect some 15 mm at the center of its 4 m span, compared to ~2 mm in a fixed-restraints case. The deflections could be reduced by adding intermediate supports to decrease the effective span of the tube. Unlike conventional receivers, in which intermediate supports would cause additional shading, the SunTrap design allows support brackets (identical to that shown in Fig. 5) to be introduced at any position along the receiver length with no optical penalty. Intermediate supports transfer load from the tube to the shell, thus taking advantage of the structural capacity of the shell. Thus, the shell itself had to be sufficiently stiff to limit deflections of the entire receiver assembly. FEA models of the sheet metal shell indicated that this rigidity was readily attainable if the open edges of the shell were constrained from warping or splaying out by means of intermittent stiffening brackets, which doubled as the absorber tube supports (Figure 5).

The thermal test prototype was scaled around an absorber diameter of 44.5mm (1-3/4in) OD to facilitate the proprietary coating deposition process. For benchmark paints such as Pyromark and LO/MIT, any size tube can be coated by spraying, but furnace constraints made this smaller scale more practical in the short term. The reduced diameter does not impact test results, as we can validate heat loss models against the test data and directly translate the results into alternative geometries with the validated simulations. In terms of structural support, the thermal test prototype receiver shell is supported by brackets in a rotating frame, while the absorber tube (and internal heater assembly) is supported by a pair of brackets (as in Figure 5, with ceramic spacers) at 1/3 and 2/3 of its length.

Task 2 – High Temperature Receiver Prototype Build

Subtask 2.1 – Prototype Fabrication and Assembly

NT's two test receivers were based on the same core geometry, scaled and adapted as appropriate for the heat loss and optical efficiency test. NT performed a steady-state heat loss test based on the NREL protocol (*Burkholder and Kutscher 2009, Heat Loss Testing of Schott's 2008 PTR70 Parabolic Trough Receiver, NREL/TP=550-45633*) and an on-sun optical efficiency test with a fluid loop. The thermal test receiver included a high performance, air-stable, solar-selective coating, and was supported and insulated as realistically as possible to simulate heat losses in operating conditions. The optical test receiver operated at relatively low temperatures (50 ˚C peak fluid *T*), so its construction was geometrically faithful but otherwise simplified, with generic insulation material and Zynolyte black stove paint rather than custom-fabricated microporous insulation and coatings.

Thermal Test Receiver

NT successfully built its second-generation thermal test receiver, shown in Figure 6.

As part of the coating development, NT is working to ensure quality control of surface preparation for a proprietary multilayer solar-selective coating with excellent air stability and optical properties, and is exploring different polishing processes and advanced surface finish characterization services.

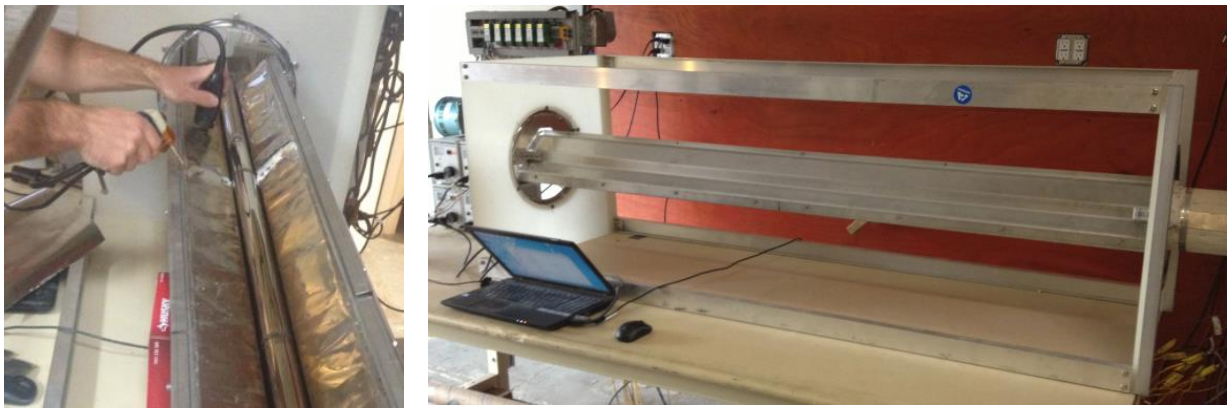

Figure 6– (Left) Assembly of thermal test receiver, spot-welding foil to enclose insulation. Tube in image is coated with an IR reflector layer. (Right) Assembled receiver in rotating frame for testing.

Optical Test Receiver

With careful planning and coordination, NT constructed the optical test receiver (shown in Figure 7) in a relatively straightforward process. For this prototype, a low-temperature application, NT opted to fabricate the insulation from commercially-available calcium silicate blocks and pipe-sections, rather than custom microporous shapes that are more expensive and have longer lead-times. The insulation shapes were readily cut with a tablesaw and assembled with manufacturer-supplied adhesive putty, which was also used to seal the exposed surfaces of the assembled shapes. NT applied stainless-steel foil tape to the exposed surfaces of the insulation to emulate the foil encapsulation on the thermal test receiver. During initial on-sun testing, however, both the adhesive on the foil tape and the calcium-silicate bonding putty succumbed to the concentrated solar beam, with substantial offgassing and browning. In response, NT stripped the foil tape and putty from the optically-active faces of the insulation and sprayed them with LO/MIT II aluminum paint to control dust and provide a diffusely-reflective surface. The diffuse surface ultimately proved useful as an observational aid during optical-efficiency testing, as beam spillage was much more visible on the paint than on the mostly-specular foil. Prior to applying the Zynolyte coating, the ends of the optical test absorber tube were threaded for convenient attachment of hose fittings connecting to the rest of the fluid loop.

Figure 7 - Optical prototype receiver and collector assembly during an on-sun test.

Task 3 – High Temperature Receiver Prototype Testing

Subtask 3.1 – **Thermal Performance Test**

Test Design

NT continued to use the NREL benchmark test protocol for heat loss testing (*Burkholder and Kutscher 2009, Heat Loss Testing of Schott's 2008 PTR70 Parabolic Trough Receiver, NREL/TP=550-45633*) employed in previous work. In this test, heat loss is measured by recording steady-state input power to a set of heaters sleeved inside the absorber tube at a given absorber temperature. The test stand (Figure 8) consists of the heater assembly (mounted inside a copper tube to smooth the heat distribution to the absorber), a set of variacs and variable-output power supplies, a bank of power transducers, and an array of thermocouples to monitor absorber temperature. The receiver prototype is mounted in a frame that allows rotation in order to measure heat loss across the operational range of tilt angles.

Figure 8– NT heat loss test stand during test. Receiver is mounted in rotating frame on lazy-susan bearings to facilitate testing over a range of tilt angles.

In this second iteration, NT revised the test stand to improve data quality and ease of construction, with increased density of thermocouples on the absorber tube and a redesigned heater assembly.

Initially, NT re-commissioned the heat loss test stand with upgraded controls and instrumentation. Notable changes included: additional power supplies to permit independent control of end boundary-condition heaters, more thermocouples on absorber tube to better map temperature distribution, and shielding improvements to reduce noise in thermocouple readings.

Additionally, NT redesigned the heater core system to eliminate machining of the absorber tube in order to support the heater assembly and the use of bolt-on thermocouples on the absorber (incompatible with the proprietary coating process) and to provide additional support for the heater assembly to reduce sagging when the copper tube is softened by high temperatures. In NREL's thermal test stand heater assembly (see http://www.nrel.gov/csp/troughnet/pdfs/2007/41429.pdf), swaged thermocouples are routed along the internal copper tube (containing the heater assembly) and then bent such that they contact the ID of the absorber tube. The success of this method depends on the thermocouples being thermally coupled to the absorber tube rather than the copper tube, and in good thermal contact with the absorber. The former concern is mitigated by lightly insulating the copper tube near each thermocouple junction, while the latter is more difficult. NT modeled the thermal system of the thermocouple within the absorber tube and concluded that the junction temperature should be well-staked to the absorber tube by positioning alone, without relying on direct conductive contact between TC and tube. As an aside, the switch to swaged, isolated-junction thermocouples enabled substantial electrical noise reduction compared to the previous exposed-junction, bolt-on TCs.

NT ran preliminary testing of the revised heater assembly by fully enclosing the absorber tube in calcium silicate insulation. This test setup enabled initial uniformity corrections, up to the point at which the insulation itself introduced more temperature nonuniformity than the heater and thermocouple assembly. In this trial assembly, NT tested thermocouple contact with the absorber tube by applying a torch flame to the absorber near each internal thermocouple and observing the thermocouple response. Several iterations of disassembly and tuning eliminated the worst outliers, but NT's general experience is that simply bending

thermocouples such that they are spring-loaded into contact with the absorber ID produces inconsistent contact conditions that affect data quality. Local application of a torch flame worked to check contact after assembly, and pulse heating of the internal heaters identified any thermocouples that were overly coupled to the copper tube, but NT observed little difference in setup between thermocouples that showed good vs. fair coupling to the absorber tube. That is, it was difficult to ensure good thermal coupling during preparation of the heater assembly, in that similarly-configured thermocouples would not necessarily perform similarly once the heater assembly was sleeved into the absorber tube. NT suspects that much of the difficultly stems from using a small-diameter tube (constrained by current coating equipment) of 1.5 inch ID in this prototype iteration as opposed to the ~2.6 inch ID tubes that NREL had tested. This narrow diameter, paired with a 1in OD copper tube to distribute heat flux from the internal cartridge heaters, results in a radial clearance of only ~0.2 inches in which to route, bend, and position thermocouples. Small radial clearance reduced the options to optimize the thermocouple bend scheme, as well as making thermal isolation from the copper tube more challenging. Overall, the bent-thermocouple scheme was workable for testing but far from ideal from an assembly and data-quality perspective. NT hopes to resolve these issues in future testing.

Due to coating equipment limitations, the tubes are ~18 in long, such that four tubes must be joined end-to-end in order to form the full prototype assembly. NT designed a system of internal couplers (stainless steel tubing slit lengthwise) to structurally connect the short tubes into a contiguous absorber (Figure 9). These couplers provide attachment points for internal thermocouples (spot-welded to the ID of the couplers) with consistently good thermal contact to the absorber tube.

Figure 9- CAD image of absorber tube sections assembled with internal sleeve couplers to form a complete absorber. Copper pipe contains heater assembly, with absorber assembled over heater assembly to facilitate thermocouple routing. Right side half is assembled, left side shows exploded view of components in order of assembly.

Test Results

The thermal prototype absorber tube is coated with a proprietary solar-selective coating. The emissivity of the coating is ~0.09 at 400 °C and has comparable performance to other state-of-the-coatings while also being air-stable up to at least 550 °C. The absorber tube is partially surrounded on by microporous insulation with an average conductance of ~0.018 W/m-K for the temperature range of interest. The insulation forms an air filled cavity below the absorber tube that is contained by AR coated glass. The stainless steel shell provides structural stability to the receiver.

Figure 11 shows the heat loss from the thermal test prototype in the required test range of 300 °C to 650 °C. The absorber temperature is determined as an average of the measurements of 4 to 6 thermocouples attached to the absorber tube along its length, corrected to an ambient temperature of 25 °C. The heat loss from the prototype is calculated as:

$$Heat\ Loss\ (W/m) = \frac{Q_{\text{cart1}} + Q_{\text{cart2}} + Q_{\text{coil1}} + Q_{\text{coil2}} + \frac{k.A}{\Delta x}(Cu1 - Cu2) + \frac{k.A}{\Delta x}(Cu3 - Cu4)}{L_{HCE}},$$

where Q_{cart1} and Q_{cart2} are the average cartridge heater powers (W), Q_{coil1} and Q_{coil2} are the average inner coil heater powers (W), k is the thermal conductivity (W/m-K) of the copper, A is the cross-sectional area (m^2) of the copper pipe, $Cu1$, $Cu2, Cu3\ and\ Cu4$ are the average temperatures of the copper tube near the ends of the prototype, Δx is the distance (m) between $Cu1$ and $Cu2$, and between $Cu3$ and $Cu4$, and L_{HCE} is the length (m) of the prototype.

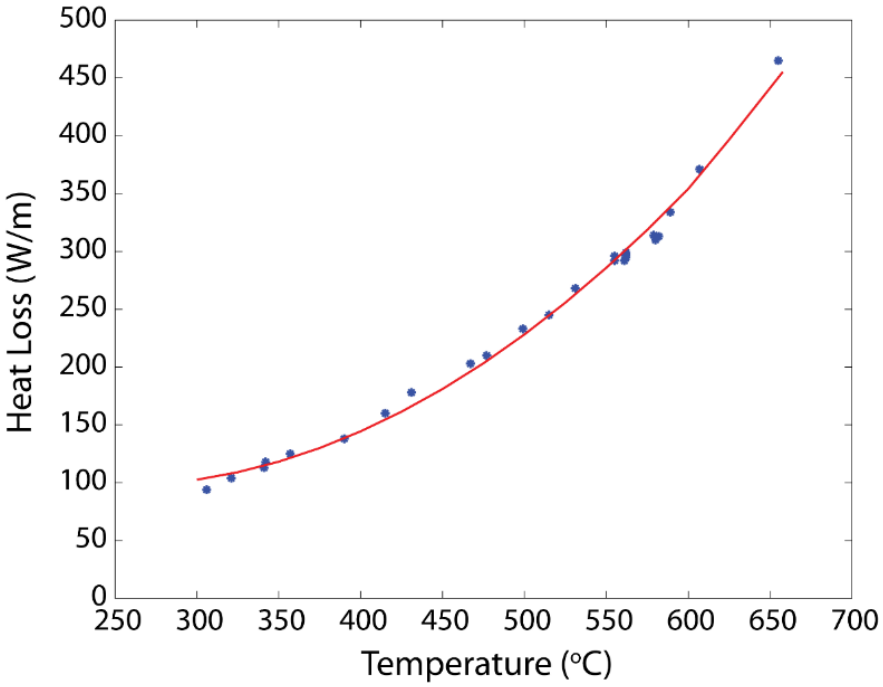

Figure 11 – Heat loss in the temperature range of 300-650 ˚C for the SunTrap receiver heat loss test prototype.

To meet the project deliverable, the thermal losses must be less than 440 W/m at an absorber temperature of 550 °C when sized for a 5 m mirror. Since the solar-selective coating is still at laboratory scale, the absorber tube diameter was limited. It is therefore necessary to scale the thermal losses for the prototype (as detailed in the full, proprietary version of the final report to the DOE). Assuming that heat loss increases linearly[1] with absorber diameter, the deliverable implies that the prototype thermal losses must be less than 302 W/m at 550 °C.

Table 1 shows the measured steady state absorber temperature versus input power. The average input power is 295 W/m with a standard deviation of 2.6 W/m and is under the required 302 W/m to a statistical significance of > 99.9%. The temperature data are used to perform a one-sided student's t-test in Table 2 that demonstrates an operating temperature of T > 550 °C for thermal losses ≤ 302 W/m at 95% C.I. (p-value < 0.05), thus meeting the deliverable.

[1] As explained in the following section, computational models suggest that the heat loss scales with absorber diameter at a rate that is less than linear and therefore the assumption of linearity may produce a more demanding heat loss target than the deliverable requires.

Table 1 – Steady-state temperature versus input power for thermal test prototype.

Temperature (ºC)	Power (W/m)	Temperature (ºC)	Power (W/m)
548	295	555	298
543	296	575	299
563	295	578	298
566	295	545	300
540	296	562	300
546	297	557	299
542	296	600	296
555	297	602	296
557	296	555	296
545	296	550	296
558	294	556	296
553	294	551	293
561	290	565	293
556	290	566	293
550	292	564	293
560	292	558	293

Table 2 – One-sided t-test calculation for receiver heat loss, using data from Table 1.

Success Value (ºC)	>550
Required P-value	<0.05
Standard Dev. (ºC)	14.211
Mean (ºC)	**558.81**
Number of Samples	32
t-value	3.507
Degrees of Freedom	31
p-value	**0.000703**

In the simplest case, the radiative heat flux from a bare absorber tube to its surroundings are given by

$$q = A_a \sigma \varepsilon_a (T_a^4 - T_{am}^4) ,$$

where q is the heat transfer, σ is the Stefan-Boltzmann constant, T_a is the temperature of the absorber tube, T_{am} is the temperature of the glass, ε_a is the emissivity of the absorber surface, and A_a and A_g are the surface area of the absorber tube. Therefore, the radiative heat loss scales with A_a. The surface area of a cylinder is given by $A_a = 2\pi rL$ where r is the cylinder radius and L is the length of the absorber tube. Assuming that the length is unchanged, the heat loss simply scales linearly with r (and not r^2.).

The 1D Forristall heat loss model (as implemented by *Burkholder and Kutscher, 2009*) is used to examine how this relationship holds up for a typical evacuated receiver. The Forristall model is run for a fluid temperature of 550 °C, under zero irradiance and at an ambient temperature of 30 °C. The emissivity of the absorber tube is 0.1225. Table 3 shows the heat loss under various geometric configurations.

Table 3 - Calculated heat loss using Forristall 1D model for evacuated receiver.

Absorber Diameter (cm)	Glass Diameter (cm)	Heat Loss (W/m)	Absorber Diameter Ratio	Heat Loss Ratio
7	12	654	1	1
3.5	6	327	0.5	0.5
1.75	3	164	0.25	0.251

Results from Table 3 demonstrate the heat loss from an evacuated receiver scale linearly with the absorber diameter, provided that the glass diameter is also scaled (the view factor between the glass and the absorber tube remains constant).

The Suntrap receiver uses a smaller active area of absorber than a typical evacuated receiver, and thus has tighter constraints on absorber diameter. For the prototype-scale receiver, the depth of air cavity was kept constant at 3cm. It is undesirable to reduce the depth of the air cavity further as doing so introduces additional thermal losses due to conductance and convection through the air. Ansys FLUENT was used to assess how changing the absorber tube while keeping the cavity depth affected the heat loss.

Table 4- Calculated heat loss using Ansys FLUENT model for SunTrap receiver.

Absorber Width (mm)	Heat Loss (W/m)	Absorber Diameter Ratio	Heat Loss Ratio
44	317	0.5	0.555
55	382	0.625	0.669
66	445	0.75	0.780
77	508	0.875	0.890
88	571	1.00	1.000
99	631	1.125	1.105
110	692	1.25	1.211

Table 4 shows the heat loss from a geometric configuration that is optimized for ease of manufacturing for an absorber temperature of 550 °C. The base configuration uses an 88 mm absorber tube. The heat loss from an absorber tube that is half the width (44 mm) has 55% of the heat loss demonstrating that the increase in heat loss with absorber diameter is less than linear.

This increased relative heat loss observed for smaller geometries is because the radiative losses from the cavity walls do not scale linearly with absorber width. For example, the radiative loss from the cavity wall is ~80 W/m for an absorber width of 44 mm compared to ~110 W/m for an absorber width of 88mm. In contrast, (as expected) the radiative losses from the exposed absorber tube and conductive losses from the insulated section of the absorber tube scale relatively linearly. While the radiative loss from the cavity walls is a feature of the prototype test, under operating conditions the cavity walls will absorb some solar insolation due to mirror inaccuracy which will largely offset any thermal loss. The importance of this heat loss/gain is an area of ongoing investigation.

Therefore, as noted in the deliverables, the assumption that heat loss scales linearly with absorber diameter produces a more demanding deliverable than model results suggest.

Comparison of model results to test data (see Figure 12) indicates that the heat loss from the prototype absorber tubes more closely matches modeled losses using emissivity measured from NT's proprietary coating coupons than model results with the PTR-70 coating emissivity. Model correspondence to test data is better at high temperatures, suggesting that conduction or other losses that scale linearly with temperature are not fully captured in the 2D model, or that materials (e.g., insulation) do not entirely match their expected thermal properties at low *T*. Above 500 °C, excellent correspondence (less than 2% relative difference) between model and experimental data is observed.

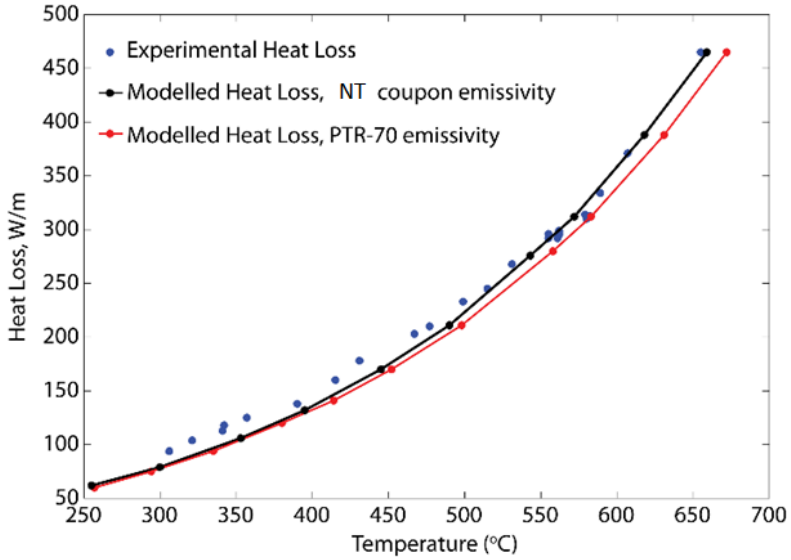

Figure 12 – Model comparison to SunTrap heat loss test data, with coating emissivity of NT coupon (see Figure 2) and of PTR-70 coating.

Subtask 3.2 – Optical Performance Test

Test Design

The optical performance test was conducted as an extension of previous NT optical test protocol, in which the receiver or a scale model thereof is tested on-sun with a trough collector, in this case the suspension collector prototype. Water is rapidly circulated through the receiver, with collected energy measured as temperature rise in the circulating water reservoir. The objective of the optical test is to verify the absorptive efficiency of the collector prototype that comprises the concentrating mirrors, suspension structure, and SunTrap receiver prototype.

High flow rate through the receiver keeps absorber temperature relatively low, reducing measurement uncertainty due to heat loss. The circulating water volume is sized to provide good temperature rise resolution, while limiting peak temperature. The increase in temperature of the fluid in the storage tank is accurately measured over the course of the experiment by using multiple thermocouples located within the tank. To characterize the system thermal capacitance and heat losses, a known heater power (~10kW) is applied to the fluid loop with the collector off-sun. Water temperature rise with a known heater power provides an accurate estimate of the effective thermal mass in the system that takes into account piping heat loss within the system. The amount of water in the system can be altered for a desired experimental time (~10-20 minutes) and insolation to achieve a sufficient temperature rise (~20-30 °C) for experimental accuracy. NT modeled heat transfer from the absorber tube to the circulating fluid and temperature rise in the reservoir, selecting a target pumping rate of ~40 gpm and a reservoir size of ~50 gal; values realized during testing were ~25 gpm and 30 gal, due respectively to flow restrictions in the piping and the desire to run multiple shorter tests in one day rather than a single long test.

Optical efficiency calculation requires measurement of both temperature rise in the fluid reservoir and beam insolation. Previously, NT had used a single pyranometer to measure total insolation, periodically shading it to record diffuse values, and interpolating these diffuse data points over the test period to estimate beam insolation. For this round of testing, NT used two pyranometers (one with a shading bar) to continuously

record beam insolation by subtracting the shaded-pyranometer diffuse insolation reading from the total insolation reading.

NT's optical test does not require active tracking, though the testing window is restricted to roughly an hour on either side of solar noon. For a typical summer/fall day in a twenty minute time span about solar noon, the solar elevation changes less than 0.1º while the solar azimuth changes approximately 11º (this is a function of NT's location in Vermont and the relatively low sun elevation at this latitude). By orientating the mirror along an E-W line, active tracking is avoided. The mirror tilt angle is manually tuned at the start of the experiment and monitored throughout to ensure that the concentrated beam from the collector strikes the center of the absorber tube. Cosine losses due to the azimuthal sweep are accounted for during data analysis; to allow for a test window of reasonable duration, the test receiver is longer than the mirror. In addition to accommodating a ~10˚ cosine angle, the extended receiver eliminates shading from the receiver support trusses. Full utilization of the mirror enables straightforward calculation of the concentrated flux on the receiver.

For the SunTrap receiver geometry, the optical performance of the receiver depends not only on glass transmittance and on coating absorptance, but also on the receiver cavity geometry and its relation to the collector. For example, for a collector rim angle of 58˚, a concentration ratio of 80, and total mirror error budget of 4.5 mrad, a bare circular pipe would achieve an intercept factor of 98.2 %. When the tube has 230˚ of its surface blocked using insulation this intercept factor drops to 94.9%. However, the cavity in the SunTrap design can act to improve this intercept factor. When the inside walls of the cavity are coated with LO/MIT high-temperature aluminum paint, with a reflectance of ~80% with over 80% of this reflectance being diffuse, the effective intercept factor increases to 96.7%. It would be beneficial in future work to test the optical performance of a bare tube and a simply insulated tube (no cavity) as well as the SunTrap receiver to assess how the cavity design impacts optical performance.

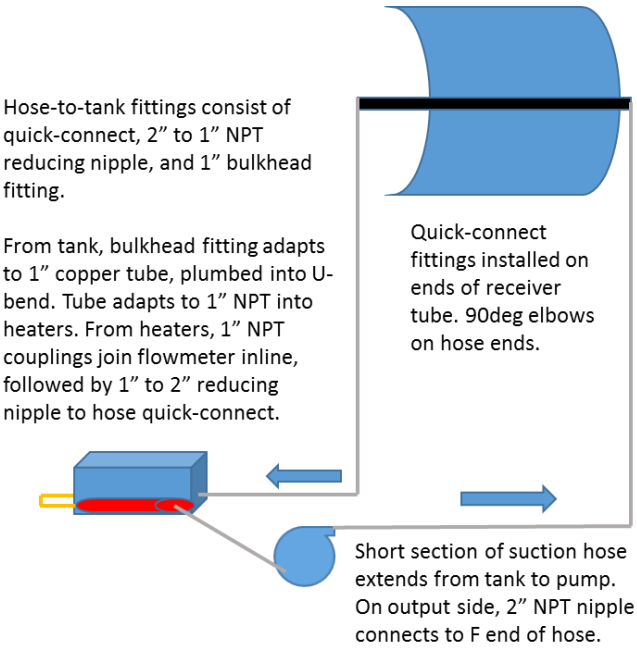

Figure 13– Optical test fluid loop piping layout. Gray lines represent 2" hose, orange 1" copper tube. Fitting detail shown in text annotations. Red cylinder alongside tank represents inline heaters for thermal capacitance calibration.

In the process of conducting the scaled-up optical test, NT gained a number of insights with regard to improving the experimental conditions:

Fluid Loop Hardware

For convenience, the optical test uses water as the heat transfer fluid. A domestic water heater was retrofitted for use as the thermal storage reservoir. NT had hoped that by plumbing the water heater in the reverse of the conventional setup, the reservoir would be well-mixed and not tend to stratify. However, initial shakedown testing revealed both poor mixing in the tank and lower-than-desired circulating flow rates due to the small-diameter water heater piping. In the water heater tank, the "straw" configuration of the hot water outlet pipe (inlet in NT's repurposed setup) inhibited mixing and created a dead zone at the

top of the tank, i.e. the inflow jet originated near the middle of the tank due to the "straw" pipe and did not effectively mix the tank volume. NT abandoned the water heater reservoir in favor of a large marine cooler, which allowed for larger piping, higher flow rates, and effective mixing of the reservoir by the inflow jet. Figure 13 shows a schematic of the water loop.

System Heat Losses

Hose and piping runs were initially left uninsulated, but as seasonal ambient temperatures fell, extraneous heat loss became noticeable in calibration data at higher temperatures. The calibration data were much improved upon adding insulation to the hoses and piping. Additionally, NT was able to largely remove heat loss effects from the calculated system thermal capacitance by using the temperature gradient when the water loop temperature matched ambient temperature. By filling the reservoir with colder-than-ambient water during calibration and testing, such that temperature rise data spanned ambient conditions, heat loss errors were minimized. When conducting back-to-back tests (before/after solar noon), NT would partially drain the reservoir and refill with an equal volume of ice water so as to resume from a cooler temperature.

Thermal Capacitance

In order to extract system optical efficiency from data of water temperature rise vs. beam insolation, a system thermal capacitance is needed. This thermal capacitance includes that of the water volume as well as that of the tank, hoses, receiver, etc. The total thermal capacitance is calculated by running the test off-sun with a known heating power applied via inline heaters. NT's previous optical test had 2.77 kW of heating power from a 120 V system, compared to an expected on-sun input power for the suspension collector of ~10 kW. Wiring the heaters to 240 V increased heater power to 10.3 kW, comparable to on-sun conditions.

Previously, variacs had been borrowed from the receiver heat loss test stand to control and measure input heater power, but these were not suitable for the power draw of the 240 V heater system. Instead, NT used a standard multimeter with current clamp to calculate heater power. Since multiple readings are required in order to establish accuracy, if NT conducts future iterations of the optical test, simplicity and accuracy could be improved with a set of power transducers similar to those used on the heat loss test stand.

The calculation of thermal capacity and optical efficiency was limited to a fluid temperature within 10° C of ambient conditions where heat loss/gain is minimal. Thermal capacity was calculated over 10 individual tests to establish statistical validity. Using these techniques, the uncertainty in thermal capacitance was reduced to 3%. The calculated thermal capacity of the system was 570 ± 20 kJ/K, which is equivalent to approximately 36 gallons of water (with 30 gal of circulating water, the thermal capacitance of and heat loss from of the piping etc. was thus comparable to 6 gallons of water).

AR-coated Glass

During shakedown, NT encountered some issues involving the glass cover on the receiver body and offgassing from the receiver system. As discussed, burning of tape adhesive and insulation bonding compound was an early problem, resulting in contamination of the glass. NT was able to clean the glass with soap and water. After a few heating cycles, the various receiver materials and paints ceased offgassing, but the calcium silicate insulation mass would still absorb moisture from the ambient air and release it as steam when on-sun. This behavior is a result of the optical test receiver being essentially unsealed; NT expects a full-scale SunTrap system to have no more issues with ambient moisture than existing Linear Fresnel receivers do. To counter this prototype glitch, NT ran the optical test on-sun without glass for ~15 min to heat up the receiver body and drive off moisture before installing the glass and restarting the test.

Test results and investigation revealed issues with the AR coating itself, discussed in the following sections.

Receiver Optical Test Results

The prototype mirror has an aperture of 4.65 m and a total active area of 15.37 m^2, with a concentration ratio of 77.1. Due to time, cost and manufacturing constraints, the absorber tube was coated with Zynolyte paint, which has a similar absorptivity (96%) to the proprietary coating. Figure 14 shows the optical efficiency test in progress with the collector and receiver on-sun.

The total thermal capacitance is calculated by running the test off-sun with a known heating power applied via inline heaters. This thermal capacitance includes that of the water volume as well as that of the tank, hoses, receiver, etc. NT's previous optical test had 2.77 kW of heating power from a 120 V system for the previous 2.2 m^2 prototype mirror, compared to an expected on-sun input power for the suspension collector of ~10 kW. By wiring the heaters to 240 V, we were able to provide 10.3 kW of heating power for better fidelity to on-sun conditions.

Figure 14 – Optical efficiency test in operation. Test cart is shown at lower right; pyranometers are visible on right side of mirror.

Early iterations of thermal capacitance and optical tests showed that the rate of increase of water temperature with time decreased as the water temperature increased, implying that heat losses from the system were significant. Accurate calculations of thermal capacity and optical efficiency require minimal heat loss. To reduce heat losses, water piping and hoses were insulated. Use of ice allowed cooling of the water reservoir to below ambient temperatures at the start of the testing. The calculation of thermal capacity and optical efficiency was limited to a fluid temperature within 10 °C of ambient conditions where heat loss/gain is minimal. Thermal capacity was calculated over 10 individual tests to establish statistical validity. Using these techniques, the uncertainty in thermal capacitance was reduced to 3%. The calculated thermal capacity of the system was 570 ± 20 kJ/K, which is equivalent to ~36 gallons of water (equivalent test stand thermal capacity of ~6 gallons of water in addition to the 30 gallons used in the circulating volume). Example thermal capacitance test data are shown in Figure 15.

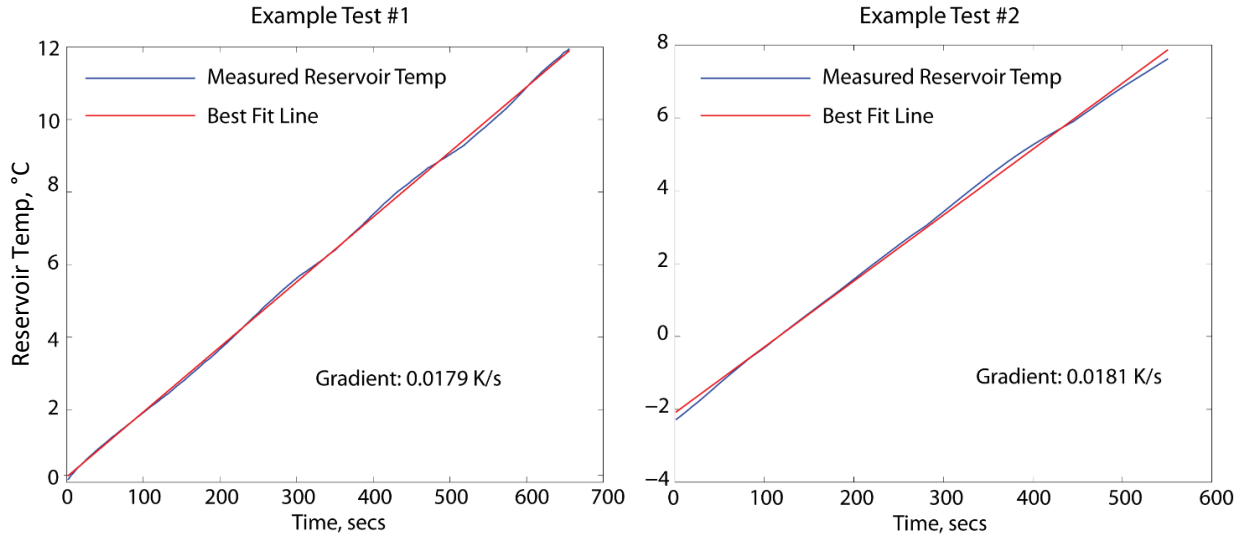

Figure 15 – Example data traces from thermal capacitance tests. Known input heater power is divided by gradient of reservoir temperature rise to yield effective system thermal capacitance.

To calculate the optical efficiency, the temperature rise of the water reservoir is measured. The total increase in the energy of the water is calculated as $E_{out} = mc\Delta T$, where mc is the thermal capacitance of the system calculated above and is 570 kJ/K. ΔT is the change in temperature of the water reservoir. The solar energy that impinges upon the mirror over the course of the test is given by

$$E_{in} = A\int_{o}^{t} I.dt \; = A.I_{\text{ave}}.t \quad ,$$

where E_{in} is the direct solar energy that falls upon the mirror, A is the mirror area, I is the instantaneous direct solar irradiance, t is time and I_{ave} is the average solar irradiance over the course of the test. The active mirror area is 15.37 m^2. The total efficiency of the system is $\eta = \frac{E_{out}}{E_{in}}$. Since the heat loss is negligible compared to the heat input owing to the low temperature (and has been taken into account in the calculation of mc), this efficiency represents the optical efficiency of the system.
A number of tests were performed with the results summarized in Table 5.

Table 5 – Optical efficiency test results. Average recorded optical efficiency is 78.32% with a standard deviation of 1.19%.

Test Number	1	2	3	4	5	6	7
Average total radiation (W/m^2)	708	751	1033	1004	922	1038	1040
Average diffuse (W/m^2)	273	242	115	187	94	90	178
Average beam (W/m^2)	435	509	918	817	828	948	862
Average Power In (W)	6685	7823	14109	12557	12726	14571	13249
Average Reservoir Gradient (K/s)	0.0092	0.0106	0.0192	0.0169	0.0179	0.0202	0.0185
Average Power Out (W)	5227	6054	10930	9647	10188	11500	10521
Est. Measurement Uncertainty (%)	5.3	5.0	4.5	4.6	4.6	4.5	4.5
Efficiency (%)	**78.2**	**76.4**	**77.5**	**76.8**	**80.1**	**79.0**	**79.4**

These data were used to perform a one-sided student's t-test to demonstrate optical efficiency of > 75% for the scale receiver-mirror system at 95% C.I. ($p < 0.05$). The calculations are summarized in Table 6 and demonstrate that the prototype mirror and receiver meet the deliverable for optical efficiency.

Table 6 – One-sided t-test calculation on optical efficiency, using test data from Table 3, demonstrating confidence in meeting optical efficiency > 75%.

Success	0.75
Required P-value	< 0.05
Standard Dev. (%)	1.19
Mean (%)	**78.32**
Number of Samples	7
t-value	7.38
Degrees of Freedom	6
p-value	**0.000318**

Measurement errors include: thermal capacitance, temperature gradient and the average beam irradiance. The measurement of thermal capacitance has an estimated error of 3%. We can assume that the temperature gradient has a similar error to the thermal capacitance while the newly calibrated pyranometers should have an error closer to 1%; with accuracy < 10 W/m^2, this gives a combined uncertainty of ~14 W/m^2. A combination of these errors yields a total measurement error of 4.5-5.3%. This error is slightly higher than the designed 4% accuracy for the test. To reduce measurement errors, the piping system would need to be overhauled to further improve mixing, flow rate, and insulation.

The receiver glass cover is of particular interest because the AR coating did not perform as expected. NT's procurement of AR-coated glass was somewhat hurried and resulted in a product that did not perform as we had been led to believe it would. The coated glass was sourced from a highly competent firm active in photovoltaics, but the product delivered had an AR coating more suitable for display applications than transmitting the energy-weighted solar spectrum as specified. NT has identified a glass and coating supplier with substantial CSP expertise for future development.

Experiments indicated that average optical efficiency with the AR-coated glass is 78%, compared to 84.7% with no glass, suggesting that the effective transmittance of the glass is 92.1%, i.e. the AR-coated glass did not perform better than the non-AR glass. While minor inaccuracies and uncertainties exist in these measurements, it is apparent that this AR coating did not adequately transmit the solar spectrum. The modelled assumption was that the glass transmitted 96% of the solar spectrum. The reason for poor performance was investigated using UV-VIS spectral analysis, shown in Figure 16, to compare the transmittance of the procured AR-coated glass and standard borofloat glass. With correctly optimized

AR-coated glass it is anticipated that the transmittance would increase to ~96% resulting in an increase in optical efficiency to 81%.

Task 4 – Suspension Collector Design

NT, Creare, and Gossamer collaborated on development of the suspension collector structure and mirror panel system. NT and Creare started with an open design space, analyzing the deflections of mirror panels of various stiffnesses to specify a target for production trials by Gossamer and Creare. From there, the suspension structure was further developed into a prototype design.

The design of the mirror involved ANSYS modeling techniques used to simulate mechanical behavior of the mirror panels and structure followed by an in depth investigation (ANSYS, SolidWorks, and custom numerical analysis scripts) into the factors that affect the deformation of mirror panels and suspension masts. The design of the suspension mirror-collector was then iterated upon by varying structural elements (e.g. torque tube stiffness, panel stiffness, mast stiffness, cable tension and stiffness) and analyzing their effect on mirror deformation and optical performance under various loading conditions. Modeling of the specific impact of mirror deformations and optical performance was established through ray tracing techniques developed by NT.

Subtask 4.1 - Suspension-Collector Structural Modeling

NT and Creare developed structural finite-element (FEA) models to analyze the collector structure under gravity and wind loads. A key early insight was that gravity loads tend to dominate mirror surface deformation; wind loads are relatively benign with regard to the mirror surface (wind torsion along the length of the drive string, however, is a major structural driver). Wind loadings (net force and moment coefficients, as well as extreme-case pressure distributions on the mirror surface) were adapted from NREL wind-tunnel data (*Hosoya et al. 2008, Wind Tunnel Tests of Parabolic Trough Solar Collectors, NREL/SR-550-32282*) on conventional troughs with an 80 degree rim angle. It is expected that wind pressure distributions and governing loads will differ somewhat for a flatter collector profile (55 degree rim angle in current analysis), but existing wind tunnel studies (*Peterka et al. 1980, Mean Wind Forces on Parabolic-Trough Solar Collectors, SAND80-7023*) have found that peak loads are neither strongly nor consistently associated with rim angle. Wind loading analysis continued as the collector design evolved, culminating in a structural model of the prototype configuration that indicated that the suspension structure could withstand 50-year design wind loads.

For initial analysis, 6 different cases were considered where the pitch angle of the collector and the wind loading were varied: 0 degrees, 45 degrees, 90 degrees, 30 degrees, 30 degrees with 5 m/s wind and 30 degrees with 11 m/s wind. For this analysis, 0 degrees indicates the collector facing vertically upwards and 90 degrees represents a collector aimed at the horizon. 30 degrees was chosen for the wind loading cases as this configuration represented a maximum wind loading configuration (*Sun et al.*, [2014], *A review of wind loads on heliostats and trough collectors, Renewable and Sustainable Energy Reviews, 32(2014) 206-221*). The deformation of the mirror and receiver support were calculated and used as inputs to optical ray tracing models.

Subtask 4.2 - Shallow-Collector Optical Modeling

NT has developed ray-tracing codes and capabilities that enable rapid analysis of the optical effects of structural deformations. The codes take as input a deflected mirror profile and/or receiver position from mechanical FEA modeling, and output optical flux distribution and geometric optical efficiency. This structural-optical model connection was crucial in defining adequate structural stiffness values for key collector elements, including the cables, cable masts, torque tube, mirror panels, and receiver supports.

The slope error of the mirror was determined by using ray tracing to calculate the deviation of the reflected light beam from the focal line owing to the deformation of the mirror at discrete locations on the mirror surface. The equivalent slope error at each discrete (or local) position is then calculated using the equation

$$fd = (2 \cdot sdx) \cdot d,$$

where fd is the local focal deviation calculated using the ray tracing, sdx is the local slope deviation and d is the distance between the local mirror surface and the focal point (e.g. *Meiser thesis, Analysis of Parabolic Trough Concentrator Mirror Shape Accuracy in Laboratory and Collector, Shaker Verlag, 2014*). The RMS slope error for each mirror configuration is then calculated. Note that this slope error contains errors due to both mirror position and gradient. Figure 18 shows example plots of calculated slope error.

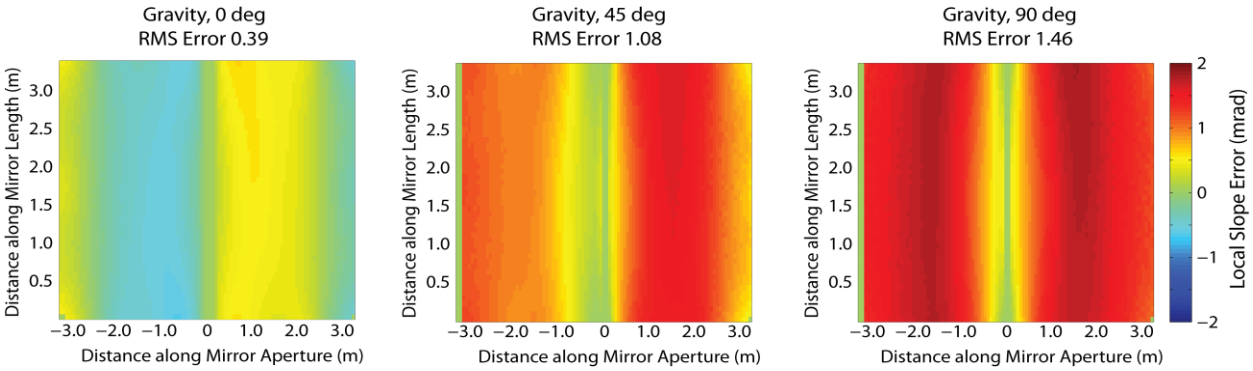

Figure 18- Mirror slope errors under gravity for 0 deg (left), 45 deg (middle) and 90 deg (right) pitch angles.

The results for each of the 6 test cases are summarized in Table 7. The RMS errors determined from the FEA and ray tracing models represent the slope error in the panels owing to deformation from the support structure under loading but neglect any slope error than is inherently present in the panel. The panels developed by Gossamer Space Frames have an RMS slope error of approximately 1.1 mrad and therefore

Table 7- Summary of mirror and mast deformation and resulting slope errors and optical efficiency for different loading conditions.

Mirror Configuration	RMS Slope Error (mrad) supports	RMS Slope Error system (mrad)	Max Mirror Deflection (mm)	Max Receiver Deflection (mm)	Optical Efficiency
0 deg	0.39	1.17	0.24	0.39	78.9
45 deg	1.08	1.54	3.04	3.99	78.6
90 deg	1.46	1.83	5.13	5.42	78.2
30 deg	0.814	1.36	1.89	2.94	78.8
30 deg + 5m/s wind	0.973	1.46	2.67	3.42	78.6
30 deg + 11m/s wind	1.66	1.99	5.82	5.32	78.2

the slope error of the system can be assumed to be $\sigma_{system} = \sqrt{\sigma_{support}^2 + \sigma_{panel}^2}$ where $\sigma_{support}$ is the slope error due to deformation of the panel from the support structure under loading and σ_{panel} is the slope error inherent in the panel. This system error represents the error due to mirror structure owing to gravitational loading and wind deflections and compare favorably to the system slope error of 2.3 mrad calculated for the Gossamer Space Frame System (*Chen et al.,* [2012] *Next Generation Parabolic Trough Solar Collectors for CSP, Proceedings of the 6th International Conference on Energy Sustainability*). This combination of errors is consistent with the errors present during testing of the mirror structure (e.g. using VSHOT) but excludes errors due to (for example) torsion, receiver alignment and tracking. These errors were expected to be small during testing of the mirror accuracy but contribute towards the optical error budget in the optical efficiency test. Under all examined load conditions to date, these modelled system errors are lower than the deliverable target of 4 mrad.

The optical efficiency of the mirror-receiver pair was calculated for each configuration. For the optical test, receiver alignment, sun tracking and torsional errors are present. Therefore, for the purposes of calculating the optical efficiency it is necessarily to estimate these errors. A ray-tracing model was used to calculate the optical performance of the SunTrap receiver. For each configuration, the rays were traced using the deformed mirror surface and displaced receiver location from the ANSYS models. An additional Gaussian scatter was imposed on the reflected ray to represent the additional errors. For the test prototype the combination of these errors can be estimated as

$\sigma_{total} = \sqrt{\sigma_{torsion}^2 + 4\sigma_{panel}^2 + \sigma_{track}^2 + \sigma_{alignment}^2}$ where σ_{panel} is the slope error inherent in the panel (~1.1 mrad), $\sigma_{torsion}$ is the error due to torsion (~1 mrad) , $\sigma_{alignment}$ is the error due to receiver alignment (~1.5 mrad), and σ_{track} is the error due to sun tracking (~1.5 mrad). These errors combine to give an additional scatter of 3.2 mrad to be applied to reflected rays.

Table 7 shows the optical efficiency of the mirror-receiver pair for each mirror loading configuration using the assumptions defined for reflectivity, transmittance, and absorptivity for additional errors of 3.2 mrad. The optical efficiency for each mirror loading configuration is above 78%, thus meeting the model target of 75% optical efficiency.

Subtask 4.3 - Develop Suspension Trough Structure

NT and Creare developed a collector structure in which stiff (structural composite) mirror panels are supported primarily by a suspension cable system. As shown in Figure 19, a central torque tube or similar structure is used to span between foundation pylons, provide torsional rigidity, and provide rigid attachment points for suspension masts. Mast structures (hollow sections or trusses) extend above and below the torque tube to provide cable attachment points. Suspension cables run from the masts to various points on the mirror surface. Opposing, pre-tensed cables provide a restoring force to resist mirror deformation under gravity as the trough sweeps through its angular range. Precisely made cables enable accurate assembly of the mirror structure in a parabolic shape.

The mirror panels are a composite structure that is formed precisely in a parabolic shape and that provides rigidity between attachment points. Mirror panels are connected to the torque tube in the center of the trough, then supported by cables at the trough lip and approximately midway between centerline and lip. Structural studies provided bounding values for the stiffness of the mirror panels and cables, as well as requisite cable pretension to prevent cables from going slack.

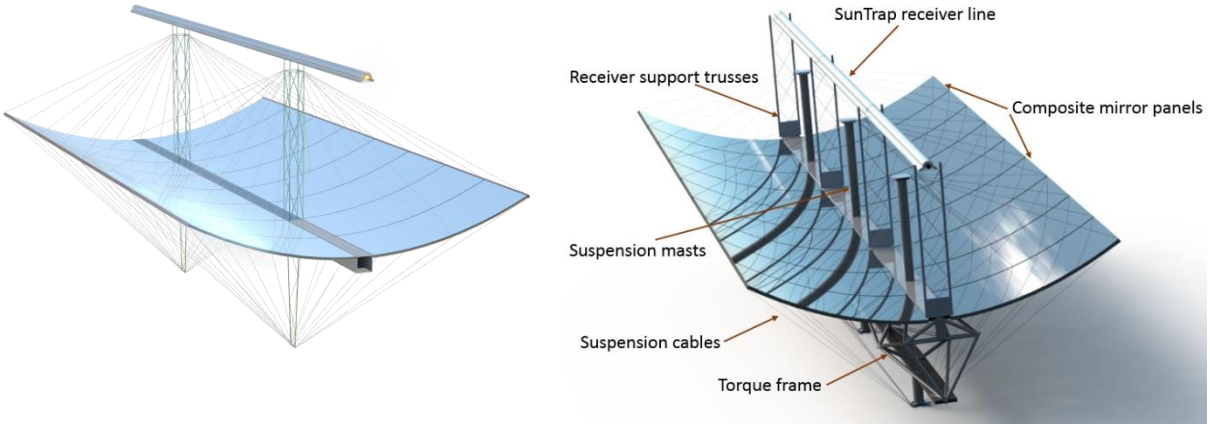

Figure 19- (Left) Draft design of suspension collector as of prototype design initiation. Highly stiff composite-backed mirror panels are anchored to torque tube at their inner edges, and supported by suspension cables at corners and midpoints. Accurate optical shape is maintained by tensioned cables on front and back of mirror. Masts provide anchor points for cables and are stiff in bending to preserve accuracy. Torque tube acts as an efficient structural backbone for the collector, resisting twist and bending in the structure to maintain alignment of receiver and mirror. Note that masts double as receiver supports, a configuration which was abandoned thereafter. (Right) Idealized suspension collector design following prototype build. Torque tube is replaced with more efficient torsional space frame, and simple trusses support receiver line. A 4m mast spacing is depicted for visual symmetry, though a 6m spacing is also feasible.

With the aperture shape of the parabola supported entirely by cables and the mirror itself, the collector frame can be reduced to a central spine that provides rigidity in bending and torsion. In order for the cable array to keep the collector aligned, the masts must be rigidly coupled to this central spine. Studies on mast stiffness identified the torque tube stiffness as a limiting factor; a 12 in square steel torque tube with 0.25 in wall thickness was identified as being a sufficient baseline member for the prototype collector to avoid excessive error in the masts. Following studies examined the twist of the torque tube along a long run of collectors (multiple spans) under a constant wind-induced moment per unit length, as well as the bending stiffness of the tube between pylons. These studies concluded, respectively, that torsional rigidity of the 12 in torque tube was sufficient only for strings extending up to ~24 m (assuming 12 m spans between pylons) beyond the tracking drive, and that bending stiffness was borderline. A torque box or similar frame could be envisioned as the next step to achieve similar or improved torsional and bending stiffness with less material usage. Alternatively, reduced length drives could be implemented to further reduce torque tube requirements and allow further material reductions.

A key design question was the axial span of collector that would be supported by a single mast assembly; for a nominal span between bearing pylons of 12 m, cases for 2, 3, and 4 masts per span were modeled. A single mast proved acceptable for supporting 6 m of mirror (at a design aperture of 5 m), corresponding to a configuration with two masts per span. The bending stiffness of the mast-to-torque-tube mounts was found to be a key factor in maintaining suspension mirror accuracy for the larger spans, and stiffening plates were added to the prototype design as a result. Double function of the masts as receiver supports

had been considered, but was deemed unsuitable as the receiver weight tends to bend the mast and thus acts to deform the mirror via the suspension cables.

Prototype Collector Design

The prototype suspension mirror-collector structure was designed to represent a subunit in a larger solar field array, with a few notable simplifications for initial prototyping. Due to the cost and time advantages of using existing forms and tooling in mirror fabrication (for mirror panels manufactured by Gossamer Space Frames), the prototype mirror aperture was set at 4.65 m (providing a rim angle of 60º at a focal length of 2012 mm), compared to the design collector aperture of 5.0 m (with focal length of 2165 mm) that was the subject of optical and loading analysis. Additionally, the prototype collector design spanned 3 x 1.2 m-wide mirror panels, rather than 5 as in the design collector. This simplification was chosen in order to avoid the complexity of accounting for receiver support shading during the optical efficiency test.

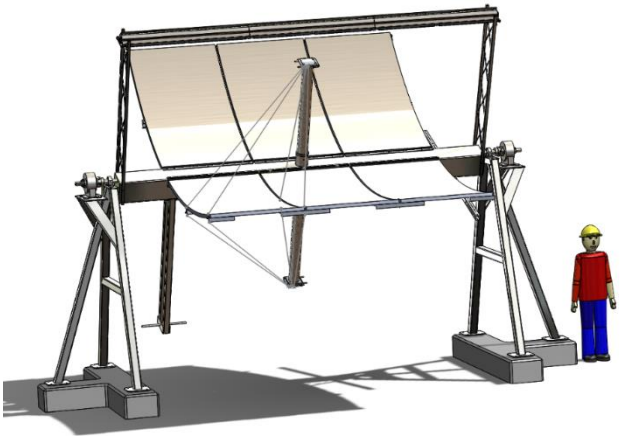

Figure 20 – CAD image of collector prototype assembly. From left, along torque tube: worm drive gearbox, receiver support truss, (on bottom) balancing arm for hanging weights to bias center of mass of assembly, mirror panels, and central mast (a continuous pipe, piercing the torque tube and aligned with set screws). One set of cables is shown for reference.

The prototype collector structure (Figure 20) was mounted on A-frame supports with pillow block bearings. Slots in the pillow block bearing mounts enabled fine alignment of the collector facing solar South, and bolts at the A-frame / foundation interface facilitated leveling the collector. NT constructed a paved pad for the collector assembly and surveyed locations for the foundation blocks, which facilitated leveling and azimuthal alignment.

Designing and testing the cable-attachment hardware for the Gossamer X-perf mirror panels was an important part of the refinement of the suspension structure. Glue joint breakage, panel delamination, and local deformations were all considered. As part of developing a solution, NT and Creare designed and tested a mount that spreads the cable forces over a large area of the composite panel. Creare conducted pull-testing on this prototype mount with greater-than-expected cable forces, finding no issues.

The construction of the Gossamer X-perf panels facilitates connections to the sheet-metal backing by inserting hexagonal bars into the X-perf. These hexagonal bars were tapped to allow mounting of brackets for cable attachment. The cable mounts selected for prototyping use aluminum plates and channels to connect a set of hexagonal bars, thus distributing cable loads over many glue joints in the panel structure. Figure 21(right) shows the interface between the rectangular torque tube and the inner edge of a mirror panel; Figure 21(left) shows a cable connector for the side / outside corner of a mirror panel.

The suspension cables selected for the prototype build (see Figure 22) are stainless-steel railing-type cables, with swaged terminations. These cables were chosen as inline turnbuckles enable fine-tuning of cable lengths to adjust mirror shape during assembly. In order to facilitate cable assembly, the upper

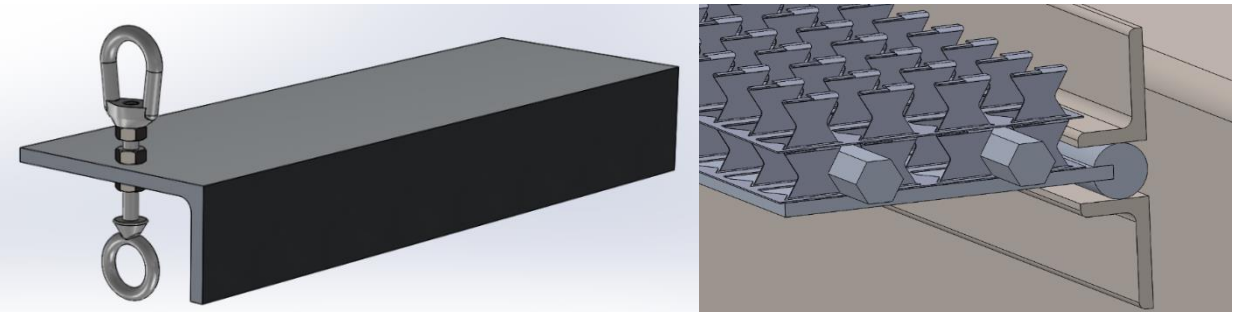

Figure 21 – (Left) Connection between mirror edge and torque tube. Tapped hex bars sleeve into X-perf structure and are linked together by plate to provide rigidity and distribute stresses. Plate is slotted into rod stock, which is captured between angles bolted to torque tube to form a "pinned" connection. Angles are adjustable to fine-tune shape of mirror. (Right) Cable connector for panel edge. Aluminum angle is bolted to hex bars in panel (not shown), with spacer washers to make up for curvature of panel. Eyebolt and eyenut provide attachment points for cable clevises, with adjustability to balance cable tension above and below mirror.

cables are 1/8in diameter, stiffly enforcing the mirror shape, while the lower cables are 3/32in, providing tension without excessively influencing the mirror shape due to the stiff upper cables.

Figure 22 – Suspension cables. Clockwise from lower left: swaged Solaflect cable for suspension heliostat, stud-terminated stainless cable for railings, and cables for prototype suspension trough. Custom cable systems are readily available from railing and marine vendors.

Subtask 4.4 - Develop Torque Transfer System

Torque transfer between structural spans of the trough (across pylons) was identified as a core design issue in initial conceptual design since it was not initially clear that a torque tube / frame would be necessary with the suspension structure. Without a torque-carrying spine in the trough assembly, rigid torque transfer from bearing shafts to the trough and suspension structure would have required a novel structure – perhaps an end truss similar to that used in the LS-3 collector. However, since a torque tube or frame structure has been identified as a necessary component of the suspension collector (the mirror panels and suspension system are not readily adapted to provide torsional rigidity), conventional torque endplates can be used to couple frame and bearing shafts. Substantive design of these features has not been conducted and is proposed as follow-on work through a reduced drive length system.

Subtask 4.5 - Optimize Structural Mirror Panels for Suspension

As suspected early in the design process, and verified through our design study, the use of a structural

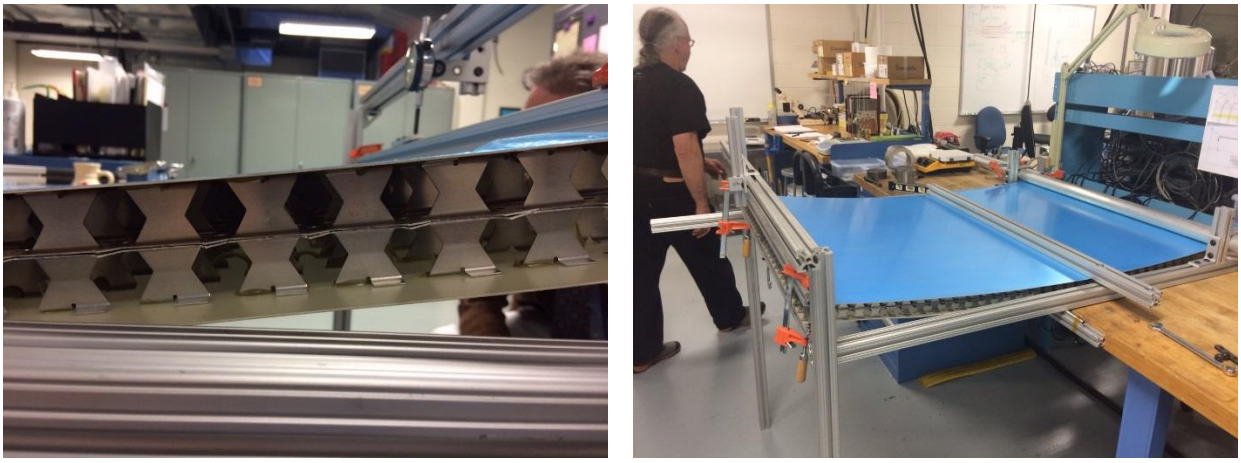

Figure 23 – (Left) Panel 3 consisting of reflective layer on G10 top sheet with double layer (bottom layer reversed) of aluminum X-perf and bottom layer of G10, and (Right) Stiffness test setup performed at Creare. Weights are added to the left side of the panel and the deflection is measured.

Table 8 – Panel stiffness test results. The stiffness of the panels with a double X-perf backing (3) is ~4x greater than the single-layer panel (1). The inclusion of a G10 bottom sheet (4) further increases the stiffness compared to panel (3) by 22%, but with a weight increase of 37%.

Panel Config Number	Top Sheet	X-perf layers	Bottom Sheet	Weight (psf)	Panel Stiffness (Nm^2)
1	Aluminum	1	None	Not measured	865
2	G10	1	None	Not measured	Not Measured
3	G10	2	None	1.01	3100
4	G10	2	G10	1.38	3800

mirror panel is a key to an optimized suspension mirror design. Mirror panel design work included: identifying appropriate stiffness and strength values for optical performance and extreme-load survival, developing a suitable (material-efficient, manufacturable, durable, weatherproof) system to achieve these structural properties, and designing connectors (as discussed previously) to hold the mirror panels and couple them to the suspension system in a rigid fashion without excessive peak stresses. NT and Creare identified a target panel stiffness based on modeling, then developed concepts for fabrication trials.

G10 (fiberglass-epoxy panel) was considered for front and back sheets of the composite mirror panels due to its high strength and stiffness along with low weight. Creare constructed a curved test panel consisting of Nomex honeycomb material sandwiched between 1/32" G10 sheets; stiffness testing showed roughly ¾ of the theoretical stiffness. While promising in terms of stiffness and weight, the Nomex proof-of-concept panel posed problems with weatherability in the long term, and with manufacturing development effort compared to Gossamer's existing X-Perf fabrication capability in the short term.

Gossamer fabricated a set of test panels using X-Perf material (aluminum sheet with bent tabs glued to a front mirror sheet). Four panels were prepared for testing: 1) A typical Gossamer panel consisting of reflective film attached to an aluminum sheet with a single layer of aluminum X-perf backing, 2) reflective film attached to a G10 sheet with a single layer of aluminum X-perf backing, 3) reflective

film attached to a G10 sheet with a double layer of aluminum X-perf backing , and 4) reflective film attached to a G10 sheet, a double layer of aluminum X-perf backing and bottom layer of G10. The stiffness of the panels was assessed by measuring the deflection of the panel under static uniaxial loading in the plane of curvature. Figure 23 shows the panel and stiffness test; Table 8 shows the results of the stiffness test.

The as-tested properties of the Gossamer test panels were used as inputs into FEA simulations performed by Creare. These results indicated that both configurations of double-layer X-Perf panels were adequately stiff to produce excellent optical accuracy in the suspension mirror. As part of optimizing for cost and performance including material usage and ease of manufacture, the G10 bottom sheet option was abandoned in favor of the simpler double layer of X-Perf. Figure 24 shows the modeled deformations of the mirror with this panel configuration at various pitch angles and wind loading. These deformations correspond to maximum slope errors of ~0.8 mrad, 1.1 mrad, 0.8 mrad and 3.3 mrad for the 0 deg, 45 deg, 90 deg and 45 deg with 84 mph wind cases respectively.

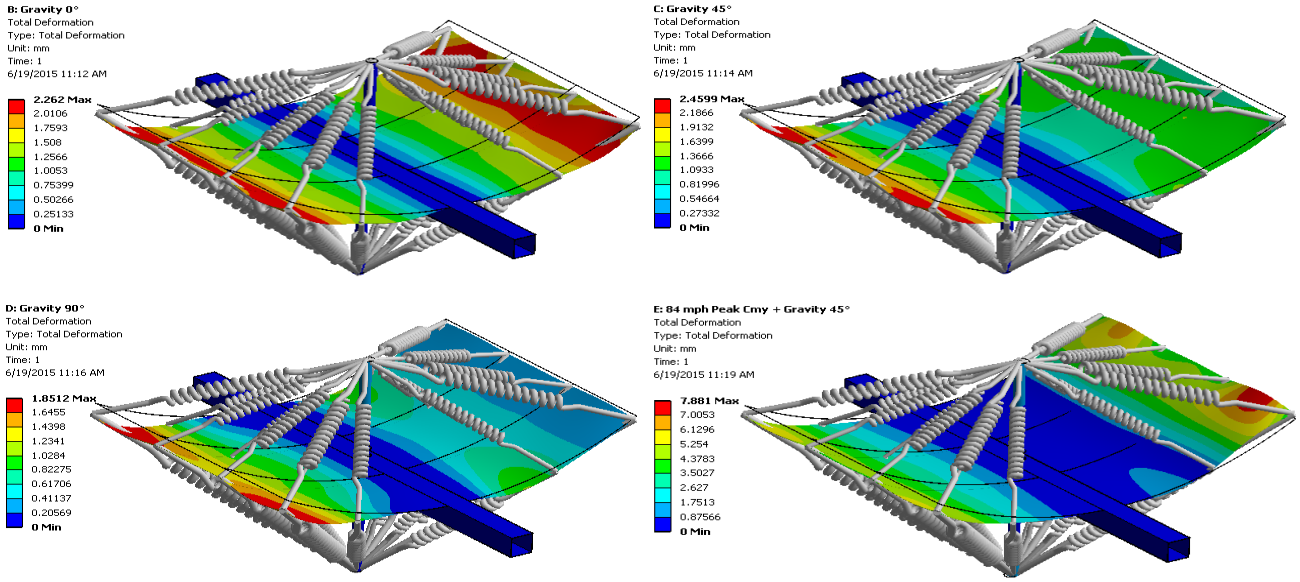

Figure 24 - Mirror Deflections for 0˚ pitch under gravity load, 45˚ pitch, 90˚ pitch, and 45˚ pitch with 84mph wind, using mirror panel stiffness from panel testing and prototype mast configuration.

The parabolic accuracy of panel 2 (single-layer G10) was estimated using photogrammetry, showing a generally good parabolic profile except for one spot in which the glue bonds had not formed in production.

While the structural performance and parabolic shape of the G10-faced panels was excellent, the mirror finish on the panels with G10 is inadequate. Figure 25 shows the mirror finish for the aluminum test panel (left) and G10 test panel with single layer of X-perf (right) after the protective film has been removed. The mirror finish on the G10 panels suffer from long-wavelength “rolling” and short-wavelength “pebbling” distortions owing to buckling of the G10 between the feet of the X-perf backing and the poor surface finish of the G10, respectively. The aluminum top sheet is stiffer (but heavier) than the equivalent G10 and therefore does not suffer from the buckling effect. The aluminum sheet is easily polished to a desired surface finish that reduces the short-wavelength pebbling distortion. Thus, the G10 system was abandoned in favor of an aluminum front sheet with double X-Perf backing, a system which was readily manufactured by Gossamer.

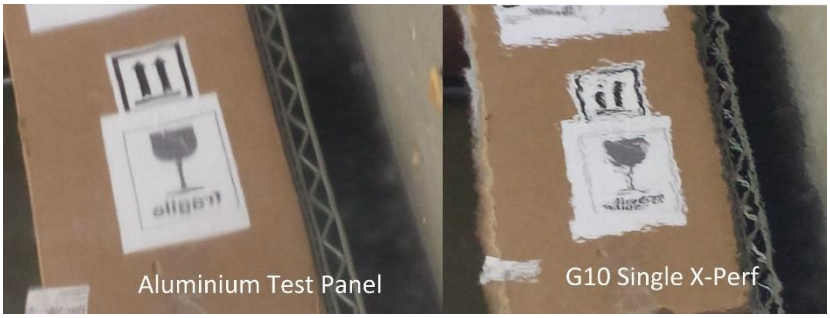

Figure 25 - Comparison of the mirror finish between the aluminum test panel (left) and G10 panel (right). Aluminum panel is far superior in optical quality; the G10 surface is unusable because of its roughness.

Subtask 4.6 - SunTrap-Suspension Collector Integration

Initial design studies including the receiver in the collector structure focused on the effects of the receiver weight, notably in causing deflections of the receiver supports. Use of the suspension masts as receiver supports was considered for structural efficiency, but this approach compounds gravity-load deflections of the mirror and receiver in that bending of the receiver support acts on the cable system and thus deforms the mirror surface. Simple plane-truss receiver supports were adopted for a low-cost, stiff solution.

Subtask 4.7 – Suspension Collector Cost Optimization

Design of the suspension collector focused on structural simplicity and material reductions. Detailed discussion of cost projections is collected under Task 7.

Task 5 – Suspension Collector Prototype Build

Subtask 5.1 – Suspension Collector and Integrated Receiver Prototype Fabrication

Figure 26 shows the assembly of the mirror collector, including the procured and fabricated elements: mirror panels, support structure, torque tube, and suspension cables with couplings and interfaces.

NT observed early in the process of tuning the collector shape that the mirror error varied from day to day even in the absence of adjustments to the prototype. The cable adjustment hardware seemed susceptible to loosening slightly under cyclic wind loading, especially if any residual twist was present in the cables. This issue is a consequence of prototyping, as NT included multiple adjustment systems in the cable system for tuning; these adjustment points have the potential to come out of adjustment. In a full-scale system, cable lengths would be factory-defined. Securely locking down adjustment and avoiding residual twist in cables resolved the issue during prototype testing.

The gravity vector appears to play a larger role than anticipated, in that the mirror shape changed noticeably depending on the collector tilt angle. Initially, NT tuned the mirror shape with the mirror at 90º; during following characterization with the mirror at 45º, NT observed an additional error of ~1 mrad, as gravity's effect on the shape of the upper half of the mirror is essentially reversed from 90º to 45º. Once cables were adjusted to optimize the mirror at 45º, this sensitivity was reduced over all tilt angles. This tilt angle sensitivity is attributed to the fact that the cables were not tensioned to level that was simulated in the design phase. NT had tested the mirror panels themselves to design cable tension levels, but some parts of our prototype cable-adjustment hardware proved susceptible to bending loads imposed by high cable tension. NT considered relatively simple hardware fixes to enable higher tension, but concluded that the accuracy change was acceptable for prototyping, given that a production system would not need such coarse adjustment features.

Figure 26 – Prototype suspension collector assembly process. Clockwise from upper left: Crane assembly of collector frame, preparing to lift torque tube; R&D technician Scott Gordon adjusting mirror edge mounts on torque tube; First mirror panel in place, showing cable connections and turnbuckles; Tracking gearbox attached to torque tube.

Task 6 – Suspension Collector and Integrated Receiver Characterization Procedures and Testing

Subtask 6.1 – Suspension Collector and Integrated Receiver Characterization Protocol and Apparatus Design

NT selected the NREL Observer method (Owkes, 2012, Stynes and Ihas, 2012) for mirror accuracy characterization, since the method offers full-surface characterization of the mirror slope error as well as receiver position error with relatively simple equipment (compared to say VSHOT). The Observer method entails photogrammetry analysis of the receiver reflection in the mirror (see Figure 27) to characterize mirror errors. The collector was characterized at a 90º pitch angle (that is, aperture perpendicular to the ground), which entailed a fixed camera tripod on the ground and was thus ideal for assembly tuning, and at operational angles with the aid of a bucket lift.

NT collaborated with NREL to check NT's code output. Originally, NT had planned to use a software package developed by NREL, but found that an editable in-house code was very helpful. The full package provided by NREL was unsuitable for the NT facility owing to differences in the NT receiver compared to a typical evacuated receiver (specifically, the glass envelope on a tube receiver provides a bright background for edge-detection of the absorber, which the NREL code relies on) and the complex reflected background owing to multiple buildings/ trees rather than a clear skyline. However, the use of individual sections of the NREL code were used to confirm accuracy of the NT calculations.

In the Observer method test, a number of photogrammetry targets are placed on and around the collector. A calibrated camera is used to take a series of photographs of the mirror reflective surface at different angles with respect to the optical axis of the collector. The photographs begin with the reflection of the absorber not visible in the collector; as the angle of the camera with respect to the collector changes, the reflection of the absorber appears on one side of the aperture and then moves across the entire aperture until it is no longer visible (see Figure 27). The series of images can be obtained by either moving the camera across the aperture of a stationary collector or by holding the camera stationary and then rotating the collector. The camera location in each of the images is determined using photogrammetry bundle analysis (see Owkes, 2012 for more details). Once the camera location for each image is known, the surface of the reflector is found in each photograph, corrected for parallax and the position of the absorber tube in the reflector surface determined. In each image the reflector-absorber errors are then calculated using the location of the camera and the location of the reflection of the absorber. The combination of the reflector-absorber errors from each image provides the reflector-absorber error for the entirety of the mirror. The uncertainty in this technique using intentional targets is ~ ±0.78 mrad and shows comparable accuracy to VSHOT/SOFAST [Stynes and Ihas., 2012].

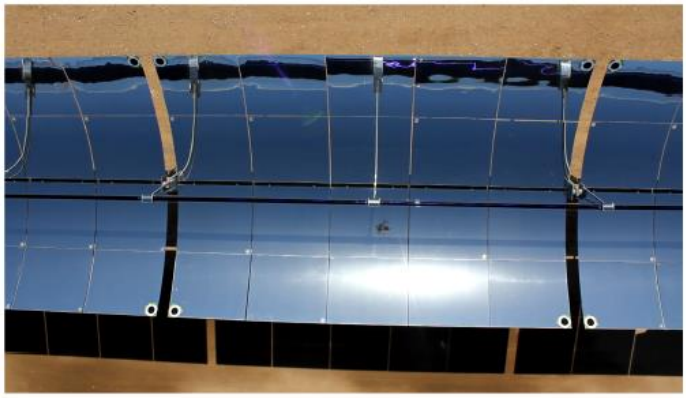

Figure 27 - NREL (*Owkes*) image of Observer technique, with absorber reflection used to calculate mirror error. Reflection of camera drone is visible above image of sun.

The errors were first evaluated at 90˚ pitch angle (aperture of mirror perpendicular to the horizon). This pitch angle represents the largest mirror error due to gravitational sag and is also the easiest to test, as the camera may be set up at the ground. The results from each test were used to guide modification of a variety of mirror structural elements such as cable length, cable tension, and absorber position.

Development of Photogrammetry Techniques for Mirror Testing and Analysis

Photogrammetry techniques to analyze panel and mirror slope accuracy were developed in-house based upon the procedures detailed in *Owkes*, [2012]. These techniques allow NT to perform examination of mirror performance independently from NREL. For initial development and testing, the mirror developed as part of NT's original SunShot award was used to develop and refine these techniques. The process to determine mirror slope error is briefly described below:

1) Multiple photographs of calibration targets are taken at various angles and camera orientations. Photomodeler software is used to determine lens distortion parameters and calibration (shown in Figure 28).

Figure 28 – Photogrammetry targets on floor and sheet of plywood, used for initial camera calibration.

2) Multiple photographs across the aperture of the mirror (e.g shown in Figure 29) are taken such that the reflection of the absorber tube in the mirror moves across the aperture of the mirror. Approximately 100 photographs per meter of mirror aperture are taken.

3) Through the placement of fixed photogrammetry targets on the mirror surface, Photomodeler software is used to perform photogrammetry bundle analysis that confirms the shape of the mirror, defines a known coordinate system relative to the mirror aperture and determines the camera position and orientation for each photograph.

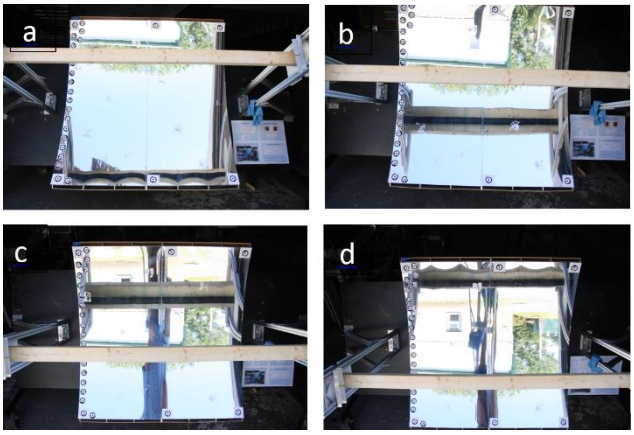

Figure 29 - Following the Observer method, photographs are taken moving across the aperture such that the absorber reflection is sampled across the mirror. Absorber reflection moves from bottom to top (a-d). This test was performed using NT's previously-developed small parabolic mirror. Board attached to backside of absorber tube provides a background to facilitate identification of the absorber edge using blob detection and removal algorithms.

4) For each photograph, a uniform grid that describes the position of the surface of the mirror is developed. This grid resolution is typically on the order of the image pixel size. The co-linearity equations, coupled with the known camera position and orientation are used to determine the position on each image (in pixels) of the uniform grid describing the mirror surface. The camera lens distortion parameters determined in step 1 are used to correct this image position from the perspective camera to the real camera (see *Owkes*, [2012] for detailed theory).

5) A new image is created that includes only the mirror surface of interest by interpolating the gray scale intensity value onto the uniform grid. This process automatically corrects the photograph for parallax.

6) A series of absorber-reflection plots are then created, with each "slice" taken at a single position along the longitudinal axis of the mirror. The number of slices generated equals the number of points along the axis of the mirror on the uniform grid. Blob detection and developed filters are used to isolate the absorber tube in the image based upon image gray-scale intensity. The required filters depend upon what other objects are reflected in the mirror. The edge of the absorber tube is determined and its centerline

calculated. The position of the absorber tube centerline may be calculated using a range of image gray-scale intensity and averaged to improve accuracy.

7) With the known position of the absorber centerline for each slice and each photograph, the surface error is calculated by $\vartheta_{ra} = \frac{1}{2} tan^{-1}\left(\frac{X_C - X}{Z_C - Z}\right)$, where X_C, Z_C are the position of the camera in the direction along the mirror aperture and the aperture normal respectively while X and Z are the position of the absorber centerline in the direction along the mirror aperture and the aperture normal respectively. This process is repeated for each slice along the mirror length to give the complete slope error of the mirror surface. This error contains errors due to both mirror shape and absorber misalignment. Absorber misalignment may be accounted for and removed from the error to give errors due to only surface deformation. More details on this process is discussed by *Owkes*, [2012].

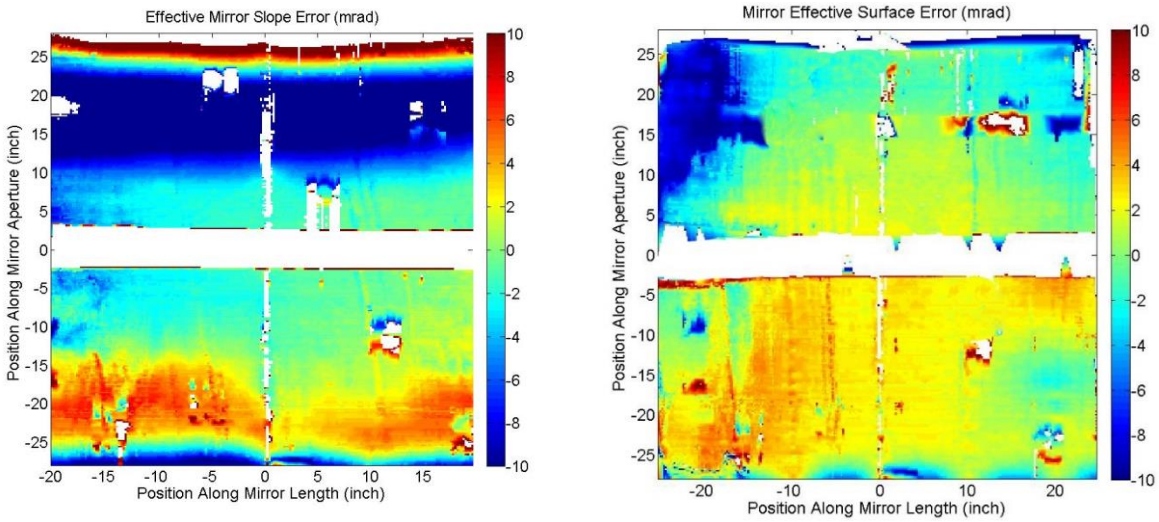

Figure 30 – (Left) Initial effective mirror slope error of the legacy prototype mirror surface from past SunShot development. Major defects are visible, associated with mirror delamination from backing ribs. (Right) Effective slope error of corrected mirror after re-mounting onto backing ribs.

The Observer process was tested using the mirror developed in an earlier SunShot award. Through analysis of the profile of light falling on the absorber tube and comparison to the optical efficiency of the system, it was previously estimated that this mirror-receiver system had an effective slope error of approximately 3 mrad. Figure 30 (left) shows the calculated optical surface error for the mirror. Data is missing at the center of the mirror owing to the thickness of the wood backboard on the absorber and at various locations on the receiver surface. This missing data is due to both the presence of photogrammetry targets on the surface and difficulties in isolating the reflection of the absorber tube in the images due to the workshop environment the mirror was tested in. Figure 30 shows that the mirror has poor performance at aperture locations of 10 to 20 inches and -15 to -25 inches where the magnitude of the effective mirror slope error becomes greater than 10 mrad. Upon physical examination of the mirror it was discovered that the mirror surface had peeled away from the supporting ribs at these locations during storage, deforming away from the ideal parabolic geometry. The RMS error of the slope surface is 6.5 mrad which is far higher than the estimate calculated during previous SunShot award work, suggesting that the mirror panel had become unglued from the supports during storage. The mirror panel was reaffixed to the suppporting ribs and retested. Figure 30 (right) shows the optical surface error after retaping the mirror surface to the supporting ribs. The optical error over the surface of the mirror is greatly improved and the RMS error reduced to 3.3 mrad. which compares favorably with the previous

estimate of ~3 mrad. This process demonstrates that photogrammetry techniques can be used to accurately characterize, analyze and improve the performance of the suspension mirror panels.

Subtask 6.2 – Suspension Collector and Integrated Receiver Characterization Testing

The Observer method test as applied to the suspension collector prototype is shown in Figure 31.

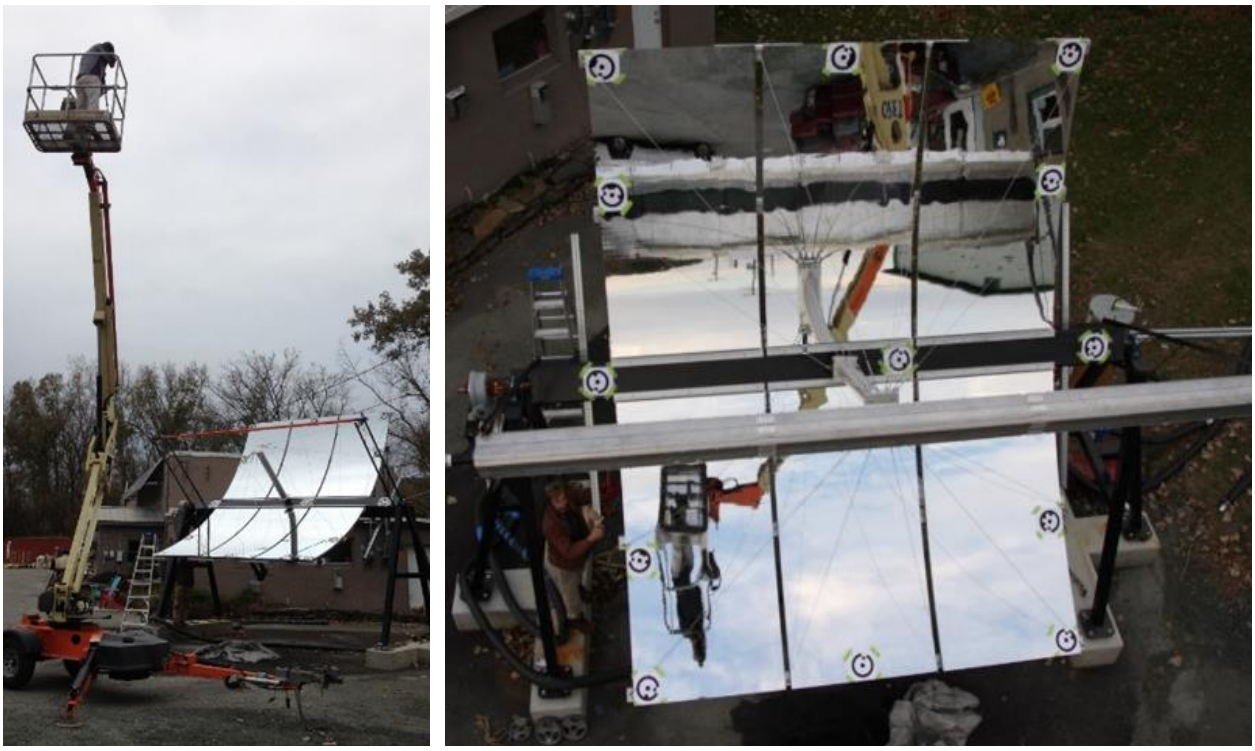

Figure 31 – (left) Photogrammetry measurement of mirror shape, using bucket lift to position camera such that mirror is at operational angle. (right) Example photograph from this method, showing reflection of absorber tube on mirror surface. Overcast sky helps with image processing accuracy.

For the bulk of mirror characterization, NT used a bare pipe in place of the SunTrap receiver, as the SunTrap shell makes isolating the mirror error from absorber position error impossible. Difficulty in isolating the bare receiver from the complex reflected background (see Figure 31(right)) made it inappropriate to use the NREL-provided code for this section of analysis. To counter this difficulty, NT painted the receiver bright orange, which allowed for a simple software filter (based upon the ratio of red to blue in the image) that accurately captured the receiver. The mirror slope error was calculated by determining the total optical error and then removing the error due to absorber position.

Initial photogrammetry measurement of the as-assembled suspension collector calculated an RMS mirror slope error of 6.5 mrad (Figure 32 (left)). An iterative process where cable lengths were altered and the mirror reexamined improved the RMS mirror slope error to 2.1 mrad (Figure 32 (right)). Fairly gross errors in the initial assembly (notably, incorrect balance of mast lengths above and below the torque tube) contributed to the high initial error.

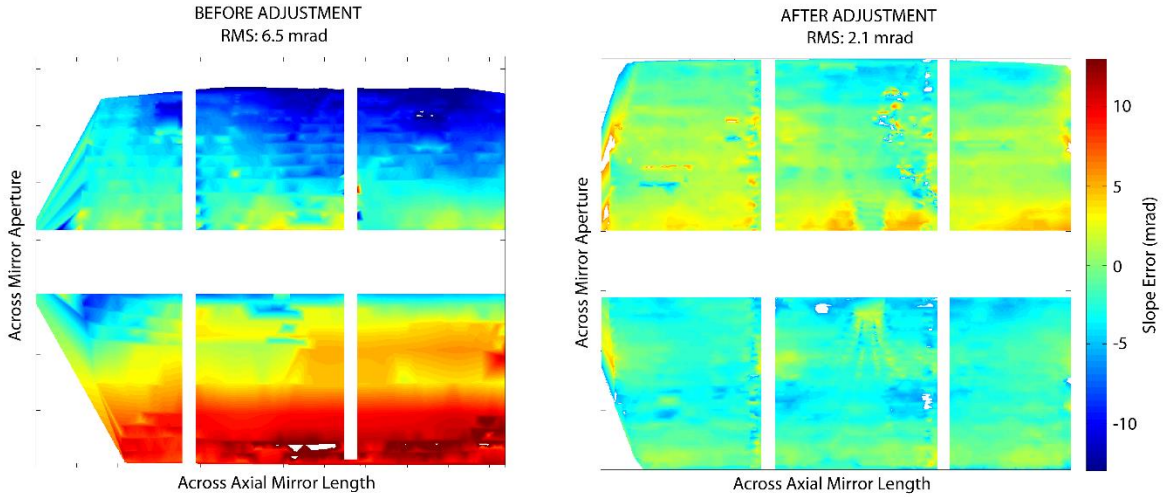

Figure 32 – Iterative tuning of mirror shape using Observer method with ideal absorber position. (Left) Mirror slope error map as-assembled. (Right) mirror slope error of 2.1 mrad after assembly corrections and tuning. Multiple test runs returned RMS slope errors of between 2.0 and 2.7 mrad.

The total system optical error was then evaluated using the SunTrap receiver. Figure 33 shows the total system optical error demonstrating an RMS error of 2.2 mrad. The close comparison between the mirror slope error and total system error demonstrates the accurate placement of the receiver. This accuracy is confirmed by the tightness of the optical beams that fall on the receiver (Figure 34).

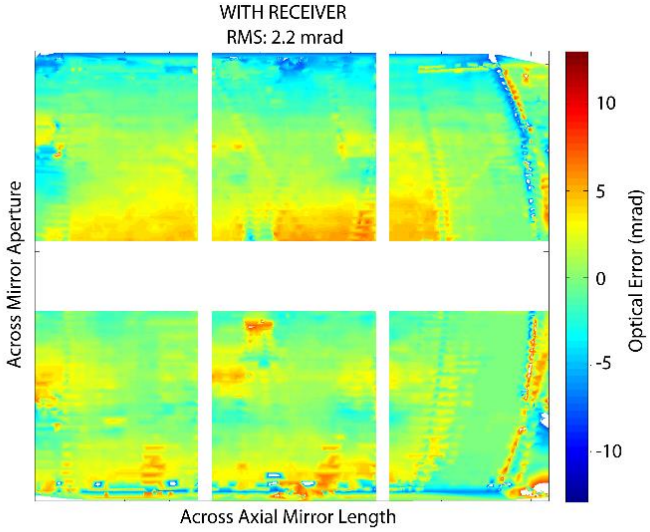

Figure 33 – Mirror slope error relative to SunTrap receiver in actual position. Comparison to error with idealized receiver position shows that NT achieved accurate receiver position by tuning mounts based on feedback from Observer method. Repeated tests yielded RMS total errors of 2.0, 2.4 and 2.9.

Modelling Efficiency of the SunTrap Collector using the Measured Slope Error

To compare results from the receiver optical efficiency test and mirror characterization, NT used the mirror slope error map as an optical model input. Gaps in the data (between mirrors, near photogrammetry targets) were filled with a Gaussian distribution using error distribution of the overall mirror. The slope error map was then used to

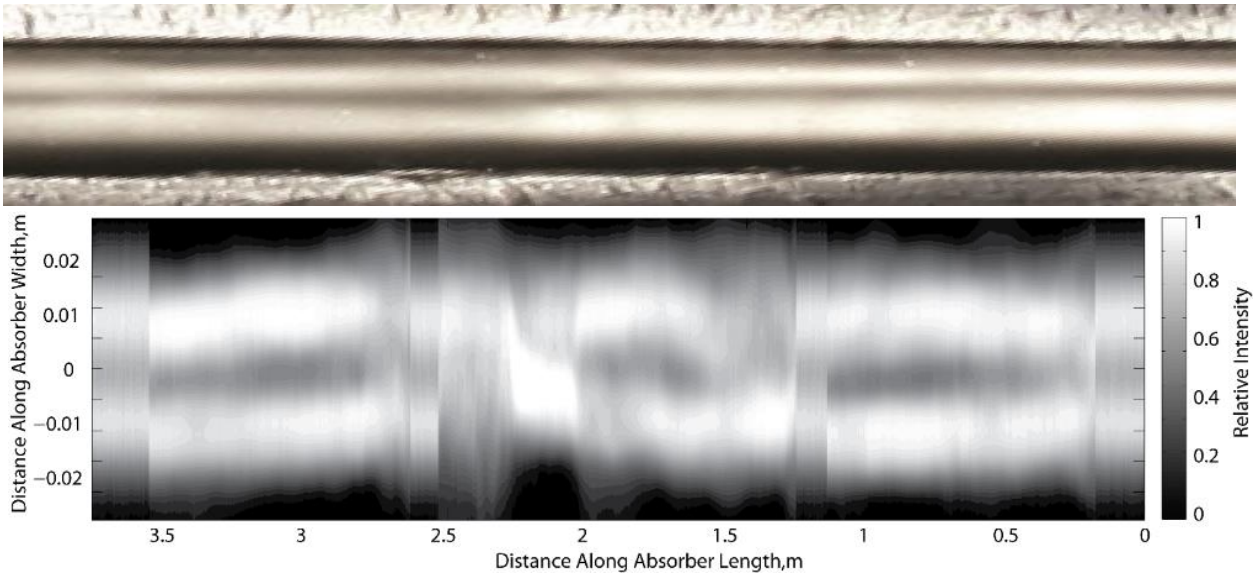

Figure 34 – (Upper) Photograph of focused beam on absorber tube. Shadow of receiver shell / central gap in mirror causes dark gap along absorber centerline. Insulation to either side of tube is painted with LO/MIT II aluminum paint, which brightly indicates any beam spillage. (Lower) Reconstruction of flux distribution on absorber tube using mirror slope error map from Observer method, processed using NREL FirstOptic technique.

calculate the optical intercept factor over the entire mirror. The intercept factor was calculated using a modified version of NREL's FirstOptic technique. The technique tracks distributions rather than individual rays that allow for significant gains in computation speed over traditional Monte Carlo techniques. NT's implementation includes the ability to calculate the power flux concentration on the absorber surface and accounts for the power gain from a single reflection from the cavity walls. Figure 34 shows the absorber tube flux distribution results from this model.

The model requires estimation of other errors: 1. Sunshape error, 2. Tilt error, 3. Receiver position error, 4. Other errors.

1) The sunshape error is calculated using the distribution described by Buie et al., 2003. For these studies a circumsolar radius of 4% was used.

2) The effective tilt error is essentially zero as the mirror is manually tilted so that the beam is centered on the absorber tube. Errors in the mirror surface and receiver position act to move the beam off the centre of the absorber tube for zero tilt error. A tilt error of -2mrad is required to center the beam on the absorber tube.

3) The SunTrap receiver is optimally positioned above the focal point. Physical measurements put the receiver approximately 15 mm above the focal point. The actual position is unknown owing to sag and variability in the absorber tube. Photogrammetry estimates of a bare tube suggest a range of 17 mm with a standard deviation of 6 mm. The absolute misalignment of the absorber tube in the direction along the mirror aperture is largely negated by manually tilting the collector to focus the light onto the tube centre. For example (for this mirror), if the absorber tube is offset from the centre of the collector by 10 mm, the beam will be centered on the absorber tube if a tilt error of -6 mrad is assumed. The optical efficiency of this configuration is virtually identical to a perfectly aligned receiver. Therefore the average offset of the receiver may be ignored. However, variability in the alignment due to sag, etc. causes variability that has a total range of 7mm (+/- 3.5 mm) and standard deviation of ~2 mm.

4) Other errors include the specularity of the mirror surface, change in mirror shape/tilt angle due to wind, changing solar circumsolar radius etc. These errors are estimated to be 1-2 mrad.

Model results suggest that the basic intercept factor of the mirror is ~97-98%. This factor is reduced owing to the presence of the mast and the masthead that is used to connect the cables to the mast. Optical models demonstrate that of the light that would hit the receiver, approximately 1% is first intercepted by the mast/masthead. Future iterations of the design would reduce the footprint of the mast and masthead to reduce the impact on optical efficiency. The best estimate for the intercept factor based upon the measured slope error is 96-97%.

The incoming radiative power is reduced due to the reflectivity of the mirror panels, the absorber absorptivity, mirror inaccuracy, and dirt on the mirror surface. The reflectivity of the mirror panels is ~94%, the absorptivity of the receiver coating is ~96%, and the reduction from dirt on the mirror is typically assumed to be 5%. This assumption is likely to be high as the mirror was kept relatively clean; 3% was used instead. The intercept factor from the optical model using the measured slope error is ~96-97%. These factors combined would yield an optical efficiency of 84.1% to 84.9%. The measured optical efficiency without glass is between 84.2-85% with a mean of 84.7%. The calculated mirror intercept factor is therefore roughly consistent with the measured optical efficiency, providing some validation of the mirror error measurement.

Patents: Awarded and Applications

A US Utility Application and an international Patent Cooperation Treaty (PCT) Application were filed based on work performed under this award. These applications were assigned the DOE-S number S-140,324.

Publications/Presentations/Travel:

Publications and presentations based on the work conducted under the award are under internal review.

Conclusion

This SunShot Incubator project has enabled NT to bring its SunTrap receiver and suspension mirror to the next level of development and to be poised to enter the market. SunTrap receiver development is now focused on manufacturability and long service lifetime with next stage development involving field testing and demonstration. Mirror development is proposed to take the next steps in partnership with Gossamer as part of a follow-on Incubator application and development work with Insolare. NT considers its most critical business risks to be those associated with supply chain, pricing and substitution, and regulatory conditions. Supply chain risks are minor for most of the SunTrap system components except for the absorber coating. NT has mitigated this risk by partnering with more than one group to develop alternate coating formulations. NT and its partners are already advancing the coating development efforts of this current project through a second SunShot grant (SolarMat2), with an emphasis on the manufacturability and longevity of the absorber coating at commercial scale. NT's objective is to develop in-house or under contract manufacturing the expertise and facilities required for the low cost high volume production of solar selective coated units.

A different risk is associated with the potential for substitution of alternate technologies, either by companies currently in the CSP industry or by new entrants. NT has demonstrated (as this report

documents) that the SunTrap system will outperform the state-of-the-art technology in terms of net thermal efficiency, and will be cost competitive. To mitigate the risk of blocked entry to the established industry, NT has pursued an ongoing strategy of building strong relationships with market participants in CSP to position the SunTrap technology—and, no less importantly, the host of sophisticated engineering expertise that NT has gained through its development—as assets mutually profitable to adopt and license. New entrants to the market pose a lesser risk to NT, which has I.P. protection for SunTrap that it is prepared to enforce; newcomers to CSP face significant barriers to entry. Given the performance advantage, developed technical expertise, extensive IP and existing relationships, NT is far more likely to be acquired by an existing market participant than to be displaced.

The strong performance of the SunTrap receiver and suspension mirror collector has been successfully demonstrated under the current award. As discussed herein, the receiver has achieved aggressive thermal loss targets of less than 440 W/m at 550 °C absorber temperature and the suspension mirror has achieved optical errors of less than 5 mrad and optical efficiencies of > 75%. This demonstrated performance well positions the SunTrap receiver and suspension mirror for strong commercial growth.

References

Buie et al, [2003] (Sunshape distributions for terrestrial solar simulations, Solar Energy, 74 (2) 113-122(10))

Burkholder F, Kutscher C. “Heat Loss Testing of Schott’s 2008 PTR70 Parabolic Trough Receiver” (NREL/TP-550-45633): NREL, 2009

Chen et al., [2012] Next Generation Parabolic Trough Solar Collectors for CSP, Proceedings of the 6th International Conference on Energy Sustainability

Cheng et al., [2014] (Comparative and sensitive analysis for parabolic trough solar collectors with a detailed Monte Carlo ray-tracing optical model, Applied Energy, 115 (2014) 559-572)

Hosoya et al. 2008, Wind Tunnel Tests of Parabolic Trough Solar Collectors, NREL/SR-550-32282

Kutscher et al. 2010, Line-Focus Solar Power Plant Cost Reduction Plan, NREL/TP-5500-48175,http://www.nrel.gov/docs/fy11osti/48175.pdf

Lupfert et al., 2001, EuroTrough – Design Issues and Prototype Testing at PSA, ASME Solar Energy Conference

Meiser 2013. Analysis of Parabolic Trough Concentrator Mirror Shape Accuracy in Laboratory and Collector. Thesis. Available at: < http://publications.rwth-aachen.de/record/229079/files/5002.pdf>.

Owkes, Jeanmarie Kathleen. An Optical Characterization Technique for Parabolic Trough Solar Collectors Using Images of the Absorber Reflection.Thesis. University of Colorado Boulder, 2012. Available at: < http://pqdtopen.proquest.com/doc/1283388816.html?FMT=ABS&pubnum=3549234>

Peterka et al. 1980, Mean Wind Forces on Parabolic-Trough Solar Collectors, SAND80-7023

Stynes, J.K. and B. Ihas (2012), Slope Error Measurement Tool for Solar Parabolic Trough Collectors, NREL Conference Paper NREL/CREP-5500-54636.

Sun et al., [2014], A review of wind loads on heliostats and trough collectors, Renewable and Sustainable Energy Reviews, 32(2014) 206-221